Scientific Reports

https://doi.org/10.1038/s41598-026-38761-8

Article in Press

Analytical evaluations using neural network-based method for wave solutions of combined Kairat-II-X differential equation in fluid mechanics

Received: 12 December 2025

Accepted: 30 January 2026

Published online: 07 February 2026

Cite this article as: Zhou P., Manafian J., Lakestani M. *et al.* Analytical evaluations using neural network-based method for wave solutions of combined Kairat-II-X differential equation in fluid mechanics. *Sci Rep* (2026). https://doi.org/10.1038/s41598-026-38761-8

Ping Zhou, Jalil Manafian, Mehrdad Lakestani, Onur Alp Ilhan, Nayier Jangi Bahador, A. A. Fattah, K. H. Mahmoud, Rzayeva Nuray & Nigar Nagiyeva

We are providing an unedited version of this manuscript to give early access to its findings. Before final publication, the manuscript will undergo further editing. Please note there may be errors present which affect the content, and all legal disclaimers apply.

If this paper is publishing under a Transparent Peer Review model then Peer Review reports will publish with the final article.

ARTICLE IN PRESS

© The Author(s) 2026. **Open Access** This article is licensed under a Creative Commons Attribution-NonCommercial-NoDerivatives 4.0 International License, which permits any non-commercial use, sharing, distribution and reproduction in any medium or format, as long as you give appropriate credit to the original author(s) and the source, provide a link to the Creative Commons licence, and indicate if you modified the licensed material. You do not have permission under this licence to share adapted material derived from this article or parts of it. The images or other third party material in this article are included in the article's Creative Commons licence, unless indicated otherwise in a credit line to the material. If material is not included in the article's Creative Commons licence and your intended use is not permitted by statutory regulation or exceeds the permitted use, you will need to obtain permission directly from the copyright holder. To view a copy of this licence, visit http://creativecommons.org/licenses/by-nc-nd/4.0/.

Analytical evaluations using Neural network-based method for wave solutions of combined Kairat-II-X differential equation in fluid mechanics

Ping Zhou[a], J. Manafian[b,c], M. Lakestani[b], O. A. Ilhan[d], N.J. Bahador[b,c,*], A.A. Fattah[e], K.H. Mahmoud[e], Rzayeva Nuray[f], Nigar Nagiyeva[f]

[a]*School of Artificial Intelligence, Wenshan University, Wenshan City, Yunnan Province, China*
[b]*Department of Applied Mathematics, Faculty of Mathematics, Statistics and Computer Sciences, University of Tabriz, Tabriz, Iran*
[c]*Natural Sciences Faculty, Lankaran State University, 50, H. Aslanov str., Lankaran, Azerbaijan*
[d]*Department of Mathematics, Faculty of Education, Erciyes University, 38039-Melikgazi-Kayseri, Turkey*
[e]*Department of Physics, College of Khurma University College, Taif University, Taif 21944, Saudi Arabia*
[f]*Faculty of Physics and Mathematics, Department of Informatics, Nakhchivan State University, Nakhchivan, Azerbaijan*

Abstract

In this paper, a symbolic computation method based on a neural network architecture, the improved neural network-based method, for obtaining novel exact solutions to combined Kairat-II-X differential equation is proposed. We secure various types of soliton solutions and periodic waves through the considered approach. Furthermore, similar to existing neural network-based schemes, this improved technique also applies the output of neural networks obtained via feedforward computation as a trial function. By introducing various activation functions, novel trial functions are extracted. These functions incorporate the neural networks' weights and biases, in that connection transforming the solution of the combined Kairat-II-X differential equation into a problem of determining these parameters. Using neural network-based technique and the improved variant, we derive a number of exact solutions including dark solitons, singular solitons, combined hyperbolic function solutions for Kairat-II-X equation. The proposed method is compared in detail with physics-informed neural networks in terms of computational theory. The physical relevance of the driven solutions is carefully examined by providing a range of graphs that show how the solutions behave for particular parameter values. Our findings suggest that they could be applied in the future to determine novel and diverse solutions to nonlinear evolution equations that arise in mathematical physics and engineering.

Keywords: Neural networks, Dark solitons, Singular solitons, Combined hyperbolic function solutions, Soliton solutions
2010 MSC: 58D19, 58J70, 65Q10

---

1. Introduction

The nonlinear partial differential equations (NLPDEs) play a crucial role in describing and analyzing various real-world phenomena across multiple disciplines, including fluid-structure interaction simulation, theoretical analysis, real-time urban wind field simulation, the physical sciences and engineering [1–5]. Its applications are observed in numerous disciplines, including control theory, physics, signal processing, solid-state physics, plasma physics, fluid mechanics, nonlinear optics, biophysics, high-energy physics, electrodynamics, quantum engineering, elastic media, chemical physics, etc [6–10]. Compared to the integer-order models, the fractional-order models provide a more accurate and comprehensive description [11]. As a result, the investigation of numerical and analytical solutions to fractional nonlinear Schrödinger equations remains a highly active research domain [12, 13].
A system is regarded as nonlinear if the change in the output is not proportionate to the change in

---

[*] Corresponding author
Email addresses: `naiyer.jangi@gmail.com` (N.J. Bahador), `nurayrzayeva@ndu.edu.az` (Rzayeva Nuray)

the input, as stated by both mathematical and physical definitions. Since most systems are intrinsically nonlinear, nonlinear problems interest engineers, biologists, physicists, mathematicians, and many other scientists. Compared to simpler linear systems, nonlinear dynamical systems, topology optimization method, which depict changes in variables over time, might seem chaotic, unsettling, or perplexing [14–18]. Stated differently, a system of equations is considered nonlinear if it cannot be resolved as a linear combination of unknown variables or functions. A system can be categorized as nonlinear whether or not the equations contain known linear functions. More specifically, even if there are nonlinearities regarding the other variables, a differential equation is said to be linear if it behaves linearly concerning the unknown function and its derivatives. Certain characteristics of the fluid that comprise a nonlinear system may appear ludicrous, unanticipated, or even chaotic [16, 19–22]. Despite appearances, such chaotic activity is not random. Nonlinear dynamical equations are difficult to solve, whereas linear equations are typically used to depict nonlinear systems [23, 24]. Over the past few years, a significant amount of work has been carried out by scientists, mathematicians, and physicists in this domain, leading to the development of effective solution approaches including the inverse scattering transform [25], the Hirota bilinear method [26–29], the enhance modified extended tanh function method [30], the improved $\exp(\Gamma(\omega))$ function method [31], the bifurcation analysis [32], the generalized tanh method [33], the multiple rogue wave solutions [34], the multiple soliton solutions [35], cubic B-splines method [36], the modulation instability analysis for coupled fractional Lakshmanan-Porsezian-Daniel equation [37], and various other sophisticated techniques [38, 39].
Myrzakulova and co-authors [40] proposed new integrable systems such as Kairat equations and Zhanbhota equation. The Kairat equations can be used in waves analysis in fluid mechanics, and optics. Among the vast spectrum of NLPDEs, the nonlinear Kairat-II (K-II) and Kairat-X (K-X) equations and its variants have emerged as paradigmatic models for understanding wave propagation in dispersive nonlinear media [40]. The Kairat equation and other forms of this equation have been extensively studied using multiple analytical approaches, including the Lie point symmetry method [41], the expa function, modified simplest equation and the generalized Kudryashov methods [42], the Riccati modified extended simple equation method [43], the Sardar sub-equation method [44]. Wazwaz et al. [45] proposed a new equation, Kairat-II-X, resulting from combining the following equations K-II and K-X, respectively as

$$u_{xt} + u_{xxxt} + 2u_t\,u_{xx} + 4u_x\,u_{xt} = 0, \tag{1}$$

$$u_{tt} + u_{xxxt} - 3(u_x\,u_t)_x = 0. \tag{2}$$

So, the combine Kairat-II-X (K-II-X) equation can be expressed as:

$$m_0\,u_{tt} + m_1\,u_{xt} + m_2\,u_{xxxt} + m_3\,(u_t\,u_{xx} + u_x\,u_{xt}) + m_4\,u_{xx} = 0, \quad u = u(x,t), \tag{3}$$

which the coefficients $m_j, j = 0, 1, ..., 4$ are real numbers whose magnitudes vary according to the specific model being investigated. When $m_0 = 0$ and $m_4 = 0$, then Eq (3) is resulted to the K-II equation. Also, if $m_1 = 0$ and $m_4 = 0$, then Eq (3) is transformed to the K-X equation. Hence, Eq (3) is combination of both equations of K-II and K-X equations. The K-II-X model describes how the principles of differential geometry of curves are related to the idea of equivalence. K-II-X equation can be utilized to survey waves dynamics in hydrodynamics, nonlinear optics, or plasma physics.
The Hirota bilinear approach [46] has been employed to present many results regarding the lump, degenerate lump, periodic wave and multiple wave solutions to some completely integrable equations [47]. In addition, the Hirota bilinear method to extract some lump collision phenomena including the spatial symmetric nonlinear dispersive wave model [48], the (2+1)-dimensional KP-BBM equation [49], the variable-coefficient generalized nonlinear wave equation [50], the generalized shallow water wave equation with variable coefficients [51], and the variable-coefficient Kadomtsev-Petviashvili equation [52]. Hirota bilinear method has been used to address various nonlinear evolution equations. Ma and Zhou presented the lump solution of some partial differential equations [53]. Ding and co-authors [54] secured lump solutions to a nonlinear partial differential equation containing a third-order derivative of time. Seadawy et al. reported some lump-type solutions, lump solutions, and mixed rogue waves to the coupled nonlinear generalized Zakharov equations [55]. Batwa and Ma [56] obtained lump solutions

to a generalized Hietarinta-type equation. Lu et al. [57] reported abundant lump Solutions alongside its interaction phenomena to the Kadomtsev-Petviashvili-Benjamin-Bona-Mahony equation. He and Zhao [58] presented some multiple lump solutions and dynamics of the generalized (3+1)-dimensional KP equation. Manafian and Lakestani [59] reported N-lump and interaction solutions of localized waves to the (2+1)-dimensional variable-coefficient Caudrey Dodd Gibbon Kotera Sawada equation.

In recent years, with the development of machine learning (ML) in different fields, scholars have begun to examine the machine learning schemes (MLSs) for solving partial differential equations (PDEs). MLSs for solving NLPDEs are divided into data-based methods and physical-laws-based techniques. Data-based techniques are such as Fourier neural operators [60], deep neural networks [61] require a large amount of high-quality simulation data. In contrast, physical-laws-based schemes remove the requirement for a lot of labeled data. Physics informed neural networks (PINNs) are one of the most promising applications of ML in scientific computing. PINNs is related to function approximations, which are trained taking into account physical laws [62]. Compared to traditional numerical methods (NMs), PINNs present important advantages in handling complex physical systems, particularly in scenarios with sparse data or large problem scales. This idea supplies greater flexibility and efficiency by avoiding the requirement for discretization of the grid. Moreover, to further accelerate network training and improve solution accuracy, various strategies have been commenced, containing the residual unit method, adaptive activation functions, adaptive loss balancing methods, and residual-based attention mechanisms [63, 64]. Liu et al. [65] introduced Kolmogorov-Arnold Networks (KANs) as promising alternatives to Multi-Layer Perceptrons (MLPs) with the emergence of PINNs. KANs completely remove linear weights, representing all parameters as spline-parametrized univariate functions. However, the aforementioned schemes are all data-driven, and the numerical solutions obtained are approximate with estimated precision.

Some methods for neural network-based (NNB) exact solution to investigate of PDE were studied by Zhang et al. [66]. The bilinear neural network method to get the exact solutions of NLPDEs for the first time was investigated in [66]. Bilinear residual networks were studied to solve nonlinear evolution in [67]. A NNB analytical solution for the Fokker-Planck and the KdV equations with trial function-based dimension reduction was obtained in [68, 69]. In [70], the fractional specialized embedding neural networks was used to obtain the exact solutions of the fractional Riccati equation into neural network architectures. The (G'/G)-expansion method along with neural network method was employed the exact solutions of the Benjamin-Bona-Mahony-Peregrine-Burgers [71].

A deep learning method, i.e., multi-term physics-informed neural networks (PINNs), to resolve forward and inverse problems of multi-dimensional hyperbolic nonlinear Klein-Gordon equations was investigated in [72]. The adaptive weight loss PINNs was proposed to obtain the solution to inverse problems of a nonlinear space-time hyperbolic sine-Gordon equation [73]. A deep learning algorithm termed PINNs was presented to resolve a hyperbolic nonlinear telegraph equation with Dirichlet, Neumann, and Periodic boundary conditions [74]. Deresse and Dufera applied PINNs and a machine learning approach for solving the nonlinear hyperbolic sine-Gordon problem [75]. An efficient neural-network-based deep learning approach and PINNs with regularization technique were used to resolve (2+1)-dimensional nonlinear damped and undamped sine-Gordon problem with variable coefficients [76]. In addition, a machine learning-based approach and PINNs were employed to investigate and explore the solution of the generalized nonlinear sine-Gordon equation with Dirichlet and Neumann boundary conditions [77].

The constant coefficient (2+1)-dimensional Graphene sheets equation was considered to explore the exact soliton solutions using the bilinear neural network method [78]. Also, the (3+1)–dimensional Bateman-Burgers equation using the bilinear neural network technique was studied in [79]. The Jacobi elliptic function expansion technique was used to obtain the exact solutions of the sixth order (3+1)-dimensional Kadomtsev-Petviashvili-Sawada-Kotera-Ramani equation in [80]. The generalized exponential rational function, modified generalized exponential rational function, and extended sinh-Gordon equation method were employed to the extended (3+1)-dimensional Kairat-X equation to find exact solutions [81].

Bifurcation, chaotic behavior, and soliton solutions of the Kairat-II equation via two analytical methods were investigated in [82]. The bifurcation, phase portraits, and exact solutions of the Fokas

equation using the improved Cham method were analyzed [83]. The novel Cham method was successfully employed to solve the (2+1)-dimensional Bogoyavlenskii's breaking soliton equations [84].
The previous studies have not sufficiently highlighted considered models. Although closed-form solutions are crucial for understanding wave dynamics, stability, and interactions in physical systems, the studies have focused on finding some analytical solutions. Therefore, the objective of this article is to extract analytical soliton solutions to the K-II-X equation expending the Neural network-based technique. This equation was first introduced and studied by various researchers who explored its mathematical properties and physical applications. Several analytical methods have been successfully applied to investigate the combine K-II-X equation, including the generalized (G'/G) method, the generalized projective Riccati equation method [85], the Kairat-II and Kairat-X equations that illustrate relations with the differential geometry of curves and equivalence aspects [86], the K-II and K-X equations in (3+1)-dimensions using new projective Riccati equation approach [87], the Kairat-II-X equation employing the Lie symmetry analysis method [88], the K-II equation and the K-X equation using the (G'/G), and the Bernoulli Sub-ODE, and the modified auxiliary equation methods [89]. We derive various soliton solutions, such as periodic, soliton-periodic, periodic, kink, anti-kink, lump, and lump soliton-periodic solitons. Therefore, the objective of this study is to conduct a comprehensive analytical and dynamical investigation of the combined K-II-X equation by exploiting the neural network-based technique to derive a broad class of exact soliton solutions. In addition to investigating the solutions, this study aims to explore the qualitative dynamics of the model through improved neural network-based technique. This integrated analytical dynamical approach provides both theoretical enrichment and practical insight into the control and prediction of nonlinear wave phenomena in the related physical models. We systematically examine the parameter dependencies of each solution type and provide physical interpretations of the observed wave behaviors. The solutions are presented through 2D plots, density plots, contour plots and 3D surface representations, offering clear visualization of the temporal and spatial evolution patterns. This study is the first to use this equation, and the diversity of the solution with the help of the method used shows an advantage for their use.
The study emphasizes the use of Maple, a well-validated software package, for computation and visualization of results, generating contour, density, 2D, 3D, and polar graphs. Strong agreement between the derived solutions and the original equation validates the findings. The versatility of the employed methods is highlighted, showcasing their ability to handle a wide range of NLPDEs. The results confirm the reliability and efficiency of the methods in providing accurate and, in many cases, novel solutions to NLPDEs. The objectives of this study were successfully achieved, yielding unique and previously unreported solutions that expand upon existing literature.
The remainder of this paper is organized as follows: Section 2 exposes the neural network-based method and its improved version. Section 3 focuses on the derivation of hyperbolic function, exponential traveling wave, periodic-singular wave, periodic wave, soliton, soliton-periodic, lump soliton-periodic and lump solutions through the neural network-based method. Finally, Section 4 provides comprehensive results and discussions.

2. Notions of Methods

2.1. Neural network-based technique

Traditional neural networks (NNs) scheme demands determining the number of layers in the NNs, the number of neurons in each layer, and the activation functions. The weights and biases parameters in the networks are initialized randomly. Input data is fed into the networks, processed through each layer of neurons, with each layer's output becoming the input for the next layer, until the final output is achieved. Meanwhile, the error backpropagation algorithm is utilized to adjust the network's weights and biases, therewith training the networks to minimize prediction errors and achieve a nonlinear mapping from input to output. In short, the neural network model contains two processes: forward propagation of information and backward propagation of errors. This paper exclusively employs the architecture of neural networks to construct novel exact solution representations and eliminates backpropagation-based training procedures. The reason is that by utilizing the structure of NNs, we can get the exact solution to the equations, thus eliminating the need to train the model through

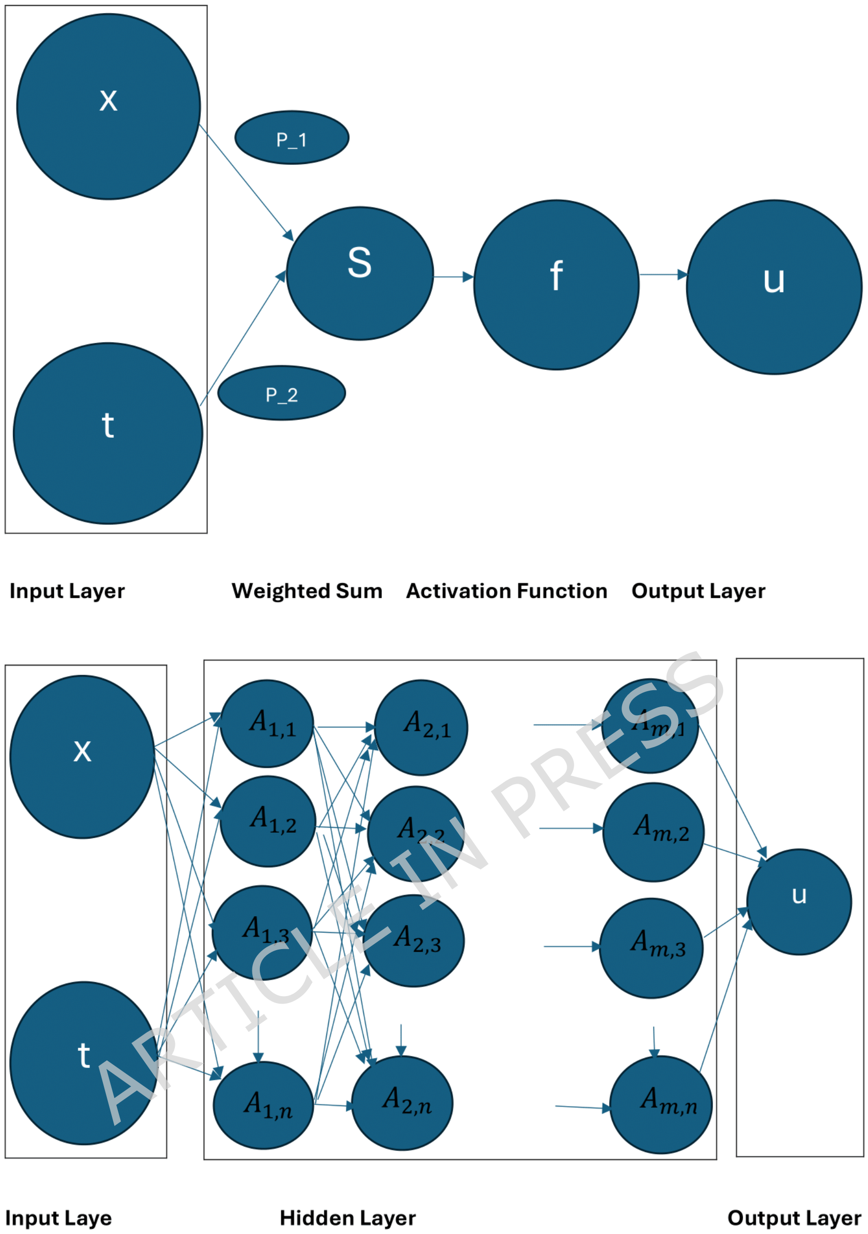

Figure 1: (Upper) Diagram of the neuron with three inputs and one output. (Bottom) Architecture of the improved neural networks.

backpropagation. A NNs architecture typically composts of multiple layers: an input layer, one or more hidden layers, and an output layer. Each layer contains multiple neurons. Each neuron is connected to other neurons in adjacent layers, with an associated weight and bias. The following Fig. 1 (Upper) illustrates a typical neuron model with three inputs and one output. The input vectors $x = (x_1, x_2, x_3)$ are propagated through weighted synaptic connections. The lines with arrows between the inputs and the neuron represent these connections. Each connection has an associated weight, which modulates the input signal. Each input is associated with a weight, denoted as p_1, p_2, and p_3. These weights determine the strength of each input's contribution to the neuron's activation. The neuron computes a weighted sum of its inputs. This S is calculated as

$$S = p_1\,x_1 + p_2\,x_2 + p_3\,x_3 + c, \tag{4}$$

where c symbolizes the bias term. This weighted summation is subsequently transformed by an activation operator, which can be a simple threshold function, a sigmoid function, a hyperbolic tangent function, or any other nonlinear function suitable for the task. The activation function processes the weighted sum and produces an output

$$u = f(S) = f(p_1\,x_1 + p_2\,x_2 + p_3\,x_3 + c), \tag{5}$$

which is the final result of the neuron's computation. The above model may be further extended to incorporate additional inputs, diverse activation functions, and intricate inter-neuronal interactions across multiple layers therewith constructing a fully functional NNs. The output of each neuron is formulated as an explicit mathematical representation, thus enabling the derivation of an explicit model for the entire network. To enhance clarity, we present this NNs model in Fig. 1 (Bottom). Furthermore, Fig. 1 (Bottom) shows the neural network contains m hidden layers and n neurons per hidden layer. The output of the j-th neuron in the i-th hidden layer can be expressed as:

$$A_{i,j} = f(p_{1,j}^{i-1}\,A_{i-1,1} + p_{2,j}^{i-1}\,A_{i-1,2} + \dots + p_{n,j}^{i-1}\,A_{i-1,n}), \tag{6}$$

which $A_{i-1,1}$ is the output of the first neuron in the $(i-1)$-th layer, $A_{i-1,n}$ is the output of the n-th neuron in the $(i-1)$-th layer, $p_{1,j}^{i-1}$ is the weight between $A_{i-1,1}$ and $A_{i,j}$, $p_{n,j}^{i-1}$ is the weight between $A_{i-1,n}$ and $A_{i,j}$. In particular, if $i = 1$, the output of j-th neuron can be expressed as:

$$A_{1,j} = f(p_{x,j}\,x + p_{y,j}\,y + p_{t,j}\,t), \quad or \quad A_{1,j} = f(p_{x,j}\,x + p_{t,j}\,t). \tag{7}$$

In contrast to traditional NNs, the overall network output is defined as either a weighted sum or a weighted product of the final-layer neuronal outputs. This design corresponds to various forms of novel exact solutions. The following trial function of u is formulated as:

$$\begin{cases} u = p_{1,u}\,A_{m,1} + p_{2,u}\,A_{m,2} + \dots + p_{n-1,u}\,A_{m,n-1} + p_{n,u}\,A_{m,n}, \\ u = p_{1,u}\,A_{m,1} \times p_{2,u}\,A_{m,2} \times \dots \times p_{n-1,u}\,A_{m,n-1} \times p_{n,u}\,A_{m,n}. \end{cases} \tag{8}$$

Here, the explicit model of NNs is employed as the trial function. The specific steps of this technique are outlined as below:

Step 1 Specify the NNs architecture, including the number of hidden layers, the number of neurons per layer, and the types of activation functions.

Step 2 Formulate the explicit expression u based on the network architecture, then substitute this expression into the governing equation.

Step 3 Arrange the equation into polynomial form, extract the coefficients of each term, and set them all to zero to obtain the system of nonlinear over-deterministic algebraic equations.

Step 4 Solve the system of equations to obtain the constraints among the weight coefficients, and substitute these constraints back into the explicit solution based on the NNs to retrieve the exact solution of the equation.

Remark 2.1 Network architectures are classified according to hidden layer count and neuron distribution. For instance, a 2-2-1-1 network denotes an architecture comprising two input neurons, two hidden layers (with 2 and 1 neurons, respectively), and one output neuron.

Remark 2.2 Network design emphasizes hidden layer neuronal counts and activation function selections, which should be tailored to the equation's initial and boundary conditions.

Remark 2.3 In order to improve the convenience of the proposed analytical method, all computations are performed with the aid of computer code written in Maple software.

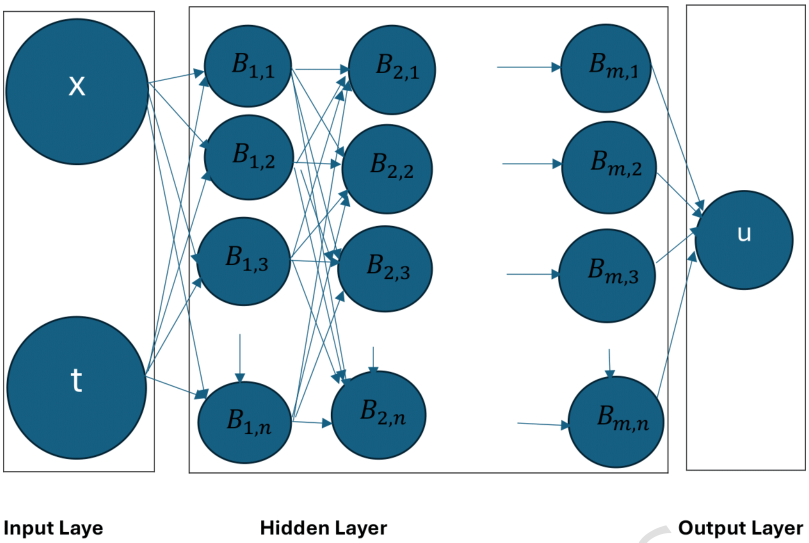

Figure 2: Architecture of the improved neural networks.

2.2. Improved neural network-based technique

The Kolmogorov-Arnold Networks (KANs) was proposed in 2024 by Liu et al. [65], which have attracted significant attention. According to Kolmogorov-Arnold representation theorem, if f is a multivariate continuous function on a bounded domain, then f can be written as a finite composition of continuous functions of a single variable and the binary operation of addition. For a smooth $f : [0, 1]^n \longrightarrow \mathbb{R}$, is given as

$$f(x_1, x_2, ..., x_n) = \sum_{l=1}^{2n+1} B_k \left(\sum_{k=1}^{n} \theta_{k,l}(x_k) \right), \tag{9}$$

which $\theta_{k,l} : [0, 1] \longrightarrow \mathbb{R}$ and $B_k : \mathbb{R} \longrightarrow \mathbb{R}$. In a sense, they presented that the only true multivariate function is addition, since every other function can be written utilizing univariate functions and sum. KANs have learnable activation functions on edges ("weights"). Unlike Multi-Layer Perceptrons (MLPs), KANs have no linear weights at all, that is, every weight parameter is replaced by a univariate function parameterized as a spline. Inspired by Kolmogorov-Arnold networks (KANs), we enhance the improved NNs technique by employing composite activation structures instead of traditional neurons. This idea enables simulating complex functional mappings with fewer parameters while utilizing diverse activation functions to generate more intricate and rare analytical solutions. Neurons in the hidden layer no longer rely on a single activation function, instead, they adopt new forms constructed through finite arithmetic operations (addition, subtraction, multiplication, division) and composite operations of activation functions. Let the NNs still contains m hidden layers and n neurons per layer. The mathematical expression of θ_i in the i-th hidden layer is

$$\theta_i = p_{i-1,i}\, B_{i-1}(\theta_{i-1}) + c_i, \tag{10}$$

which the input layer $\theta_0 = x, t$ and c is a bias vector whose elements are constants. B_{i-1} is a vector consisting of arbitrarily defined nonlinear activation functions B. $p_{i-1,i}$ denotes the matrix of weight coefficients between $i-1$-th and i-th hidden layer. The following trial function of u is formulated as:

$$u = p_{m,u}\, B_m(\theta_m) + c_u, \tag{11}$$

$p_{m,u}$ symbolizes the matrix of weight coefficients between m-th hidden layer and output layer. To facilitate understanding, we show this improved NNs model in Fig 2. Here, $B_{i,j}(i = 1, 2, ..., m, j = 1, 2, ..., n) \in B_i$ and $\theta_{i,j}(i = 1, 2, ..., m, j = 1, 2, ..., n) \in \theta_i$.

3. The combined Kairat-II-X differential equation

The Kairat-II-X equation is expressed as:

$$m_0\, u_{tt} + m_1\, u_{xt} + m_2\, u_{xxxt} + m_3\,(u_t\, u_{xx} + u_x\, u_{xt}) + m_4\, u_{xx} = 0, \tag{12}$$

in which $u = u(x,t)$ gives the wave field. This section uses a two-hidden-layer NNs to address the combined Kairat-II-X equation.

Definition 1. Let $p_{x,i}, p_{t,i}, i = 1, 2$ and $p_{i,j}, p_{j,u}, i = 1, 2, j = 3, 4$ be the weight coefficients and the activation functions to be determined are $F_i(P_i)(i = 1, 2, 3, 4)$, and also $c_i, i = 1, ..., 5$ are the real constants, then the 2-2-2-1 network architecture equipped with specific activation functions is given as follows:

$$\begin{cases} P_1 = x\, p_{x,1} + t\, p_{t,1} + c_1, \\ P_2 = x\, p_{x,2} + t\, p_{t,2} + c_2, \\ P_3 = p_{1,3}\, \boldsymbol{F_1(P_1)} + p_{2,3}\, \boldsymbol{F_2(P_2)} + c_3, \\ P_4 = p_{1,4}\, \boldsymbol{F_1(P_1)} + p_{2,4}\, \boldsymbol{F_2(P_2)} + c_4, \\ u = p_{3,u}\, \boldsymbol{F_3(P_3)} + p_{4,u}\, \boldsymbol{F_4(P_4)} + c_5. \end{cases} \tag{13}$$

3.1. Type 1: Hyperbolic function solutions

The first hidden layer contains two neurons, where the first neuron employs *coth* as the activation function and the second employs *tanh* as the activation function. The second hidden layer contains two neurons, both utilizing reciprocal function as the activation function. The detailed architectural specifications are summarized in Table 1. Based on Table 1, the following trial function $u(x,t)$ is written as

$$\begin{aligned} u = {} & p_{3,u}\,(p_{2,3}\tanh(tp_{t,2} + xp_{x,2} + c_2) + p_{1,3}\coth(tp_{t,1} + xp_{x,1} + c_1) + c_3) + \\ & \frac{p_{4,u}}{p_{2,4}\tanh(tp_{t,2}+xp_{x,2}+c_2)+p_{1,4}\coth(tp_{t,1}+xp_{x,1}+c_1)+c_4} + c_5, \quad tp_{t,j} + xp_{x,j} + c_j \neq 0, \quad j = 1, 2. \end{aligned} \tag{14}$$

The above solution is regarded as a trial function for the combined Kairat-II-X differential equation. Substituting Eq. (14) into Eq. (12), we systematically collect like terms with respect to the basis set $t, x, c_1, c_2, c_3, c_4, m_i, i = 0, ..., 4, p_{x,1}, p_{t,1}, p_{x,2}, p_{t,2}, p_{1,3}, p_{2,3}, p_{1,4}, p_{2,4}, p_{3,u}, p_{4,u}, \coth(tp_{t,1} + xp_{x,1} + c_1)$, $\tanh(tp_{t,2} + xp_{x,2} + c_2)$. The number of coefficients of the algebraic equation system is 66 equations, which includes

$$\begin{aligned} & 4c_4^2m_3p_{1,3}p_{1,4}^2p_{3,u}p_{4,u}p_{t,1}p_{x,1}^2 + 6c_4^2m_3p_{1,3}p_{1,4}p_{2,4}p_{3,u}p_{4,u}p_{t,1}p_{x,1}p_{x,2} + 2c_4^2m_3p_{1,3}p_{1,4}p_{2,4}p_{3,u}p_{4,u}p_{t,2}p_{x,1}^2 + \\ & 2c_4^2m_3p_{1,3}p_{2,4}^2p_{3,u}p_{4,u}p_{t,1}p_{x,2}^2 + 2c_4^2m_3p_{1,3}p_{2,4}^2p_{3,u}p_{4,u}p_{t,2}p_{x,1}p_{x,2} + 2c_4^2m_3p_{1,4}^2p_{2,3}p_{3,u}p_{4,u}p_{t,1}p_{x,1}p_{x,2} + \\ & 2c_4^2m_3p_{1,4}^2p_{2,3}p_{3,u}p_{4,u}p_{t,2}p_{x,1}^2 + 2c_4^2m_3p_{1,4}p_{2,3}p_{2,4}p_{3,u}p_{4,u}p_{t,1}p_{x,2}^2 + 6c_4^2m_3p_{1,4}p_{2,3}p_{2,4}p_{3,u}p_{4,u}p_{t,2}p_{x,1}p_{x,2} + \\ & 4c_4^2m_3p_{2,3}p_{2,4}^2p_{3,u}p_{4,u}p_{t,2}p_{x,2}^2 - 16c_4^2m_2p_{1,4}^2p_{4,u}p_{t,1}p_{x,1}^3 - 12c_4^2m_2p_{1,4}p_{2,4}p_{4,u}p_{t,1}p_{x,1}^2p_{x,2} - \\ & 4c_4^2m_2p_{1,4}p_{2,4}p_{4,u}p_{t,1}p_{x,2}^3 - 4c_4^2m_2p_{1,4}p_{2,4}p_{4,u}p_{t,2}p_{x,1}^3 - 12c_4^2m_2p_{1,4}p_{2,4}p_{4,u}p_{t,2}p_{x,1}p_{x,2}^2 - \end{aligned} \tag{15}$$

$$
\begin{gathered}
16c_4^2m_2p_{2,4}^2p_{4,u}p_{t,2}p_{x,2}^3 + 24m_2p_{1,4}^4p_{4,u}p_{t,1}p_{x,1}^3 + 72m_2p_{1,4}^3p_{2,4}p_{4,u}p_{t,1}p_{x,1}^2p_{x,2} + 24m_2p_{1,4}^3p_{2,4}p_{4,u}p_{t,2}p_{x,1}^3+ \\
72m_2p_{1,4}^2p_{2,4}^2p_{4,u}p_{t,1}p_{x,1}p_{x,2}^2 + 72m_2p_{1,4}^2p_{2,4}^2p_{4,u}p_{t,2}p_{x,1}^2p_{x,2} + 24m_2p_{1,4}p_{2,4}^3p_{4,u}p_{t,1}p_{x,2}^3+ \\
72m_2p_{1,4}p_{2,4}^3p_{4,u}p_{t,2}p_{x,1}p_{x,2}^2 + 24m_2p_{2,4}^4p_{4,u}p_{t,2}p_{x,2}^3 - 4m_3p_{1,4}^3p_{4,u}^2p_{t,1}p_{x,1}^2 - 8m_3p_{1,4}^2p_{2,4}p_{4,u}^2p_{t,1}p_{x,1}p_{x,2}- \\
4m_3p_{1,4}^2p_{2,4}p_{4,u}^2p_{t,2}p_{x,1}^2 - 4m_3p_{1,4}p_{2,4}^2p_{4,u}^2p_{t,1}p_{x,2}^2 - 8m_3p_{1,4}p_{2,4}^2p_{4,u}^2p_{t,2}p_{x,1}p_{x,2} - 4m_3p_{2,4}^3p_{4,u}^2p_{t,2}p_{x,2}^2+ \\
2c_4^2m_0p_{1,4}^2p_{4,u}p_{t,1}^2 + 4c_4^2m_0p_{1,4}p_{2,4}p_{4,u}p_{t,1}p_{t,2} + 2c_4^2m_0p_{2,4}^2p_{4,u}p_{t,2}^2 + 2c_4^2m_1p_{1,4}^2p_{4,u}p_{t,1}p_{x,1}+ \\
2c_4^2m_1p_{1,4}p_{2,4}p_{4,u}p_{t,1}p_{x,2} + 2c_4^2m_1p_{1,4}p_{2,4}p_{4,u}p_{t,2}p_{x,1} + 2c_4^2m_1p_{2,4}^2p_{4,u}p_{t,2}p_{x,2} + 2c_4^2m_4p_{1,4}^2p_{4,u}p_{x,1}^2+ \\
4c_4^2m_4p_{1,4}p_{2,4}p_{4,u}p_{x,1}p_{x,2} + 2c_4^2m_4p_{2,4}^2p_{4,u}p_{x,2}^2 = 0, \\
-2\,{c_4}^5m_3p_{1,3}p_{2,3}{p_{3,u}}^2p_{t,1}{p_{x,2}}^2 - 2\,{c_4}^5m_3p_{1,3}p_{2,3}{p_{3,u}}^2p_{t,2}p_{x,1}p_{x,2} - 4\,{c_4}^5m_3{p_{2,3}}^2{p_{3,u}}^2p_{t,2}{p_{x,2}}^2+ \\
16\,{c_4}^5m_2p_{2,3}p_{3,u}p_{t,2}{p_{x,2}}^3 + 2\,{c_4}^3m_3p_{1,3}p_{2,4}p_{3,u}p_{4,u}p_{t,1}{p_{x,2}}^2 + 2\,{c_4}^3m_3p_{1,3}p_{2,4}p_{3,u}p_{4,u}p_{t,2}p_{x,1}p_{x,2}+ \\
2\,{c_4}^3m_3p_{1,4}p_{2,3}p_{3,u}p_{4,u}p_{t,1}{p_{x,2}}^2 + 2\,{c_4}^3m_3p_{1,4}p_{2,3}p_{3,u}p_{4,u}p_{t,2}p_{x,1}p_{x,2} + 8\,{c_4}^3m_3p_{2,3}p_{2,4}p_{3,u}p_{4,u}p_{t,2}{p_{x,2}}^2+ \\
8\,c_4m_3p_{1,3}{p_{1,4}}^2p_{2,4}p_{3,u}p_{4,u}p_{t,1}{p_{x,1}}^2 + 12\,c_4m_3p_{1,3}p_{1,4}{p_{2,4}}^2p_{3,u}p_{4,u}p_{t,1}p_{x,1}p_{x,2}+ \\
4\,c_4m_3p_{1,3}p_{1,4}{p_{2,4}}^2p_{3,u}p_{4,u}p_{t,2}{p_{x,1}}^2 + 4\,c_4m_3p_{1,3}{p_{2,4}}^3p_{3,u}p_{4,u}p_{t,1}{p_{x,2}}^2 + 4\,c_4m_3p_{1,3}{p_{2,4}}^3p_{3,u}p_{4,u}p_{t,2}p_{x,1}p_{x,2}+ \\
4\,c_4m_3{p_{1,4}}^2p_{2,3}p_{2,4}p_{3,u}p_{4,u}p_{t,1}p_{x,1}p_{x,2} + 4\,c_4m_3{p_{1,4}}^2p_{2,3}p_{2,4}p_{3,u}p_{4,u}p_{t,2}{p_{x,1}}^2+ \\
4\,c_4m_3p_{1,4}p_{2,3}{p_{2,4}}^2p_{3,u}p_{4,u}p_{t,1}{p_{x,2}}^2 + 12\,c_4m_3p_{1,4}p_{2,3}{p_{2,4}}^2p_{3,u}p_{4,u}p_{t,2}p_{x,1}p_{x,2}+ \\
8\,c_4m_3p_{2,3}{p_{2,4}}^3p_{3,u}p_{4,u}p_{t,2}{p_{x,2}}^2 - 2\,{c_4}^5m_0p_{2,3}p_{3,u}{p_{t,2}}^2 - 2\,{c_4}^5m_1p_{2,3}p_{3,u}p_{t,2}p_{x,2} - 2\,{c_4}^5m_4p_{2,3}p_{3,u}{p_{x,2}}^2- \\
16\,{c_4}^3m_2p_{2,4}p_{4,u}p_{t,2}{p_{x,2}}^3 - 32\,c_4m_2{p_{1,4}}^2p_{2,4}p_{4,u}p_{t,1}{p_{x,1}}^3 + 36\,c_4m_2{p_{1,4}}^2p_{2,4}p_{4,u}p_{t,1}p_{x,1}{p_{x,2}}^2+ \\
36\,c_4m_2{p_{1,4}}^2p_{2,4}p_{4,u}p_{t,2}{p_{x,1}}^2p_{x,2} - 24\,c_4m_2p_{1,4}{p_{2,4}}^2p_{4,u}p_{t,1}{p_{x,1}}^2p_{x,2} + 28\,c_4m_2p_{1,4}{p_{2,4}}^2p_{4,u}p_{t,1}{p_{x,2}}^3- \\
8\,c_4m_2p_{1,4}{p_{2,4}}^2p_{4,u}p_{t,2}{p_{x,1}}^3 + 84\,c_4m_2p_{1,4}{p_{2,4}}^2p_{4,u}p_{t,2}p_{x,1}{p_{x,2}}^2 + 40\,c_4m_2{p_{2,4}}^3p_{4,u}p_{t,2}{p_{x,2}}^3- \\
2\,c_4m_3p_{1,4}p_{2,4}{p_{4,u}}^2p_{t,1}{p_{x,2}}^2 - 2\,c_4m_3p_{1,4}p_{2,4}{p_{4,u}}^2p_{t,2}p_{x,1}p_{x,2} - 4\,c_4m_3{p_{2,4}}^2{p_{4,u}}^2p_{t,2}{p_{x,2}}^2+ \\
2\,{c_4}^3m_0p_{2,4}p_{4,u}{p_{t,2}}^2 + 2\,{c_4}^3m_1p_{2,4}p_{4,u}p_{t,2}p_{x,2} + 2\,{c_4}^3m_4p_{2,4}p_{4,u}{p_{x,2}}^2 + 4\,c_4m_0{p_{1,4}}^2p_{2,4}p_{4,u}{p_{t,1}}^2+ \\
8\,c_4m_0p_{1,4}{p_{2,4}}^2p_{4,u}p_{t,1}p_{t,2} + 4\,c_4m_0{p_{2,4}}^3p_{4,u}{p_{t,2}}^2 + 4\,c_4m_1{p_{1,4}}^2p_{2,4}p_{4,u}p_{t,1}p_{x,1}+ \\
4\,c_4m_1p_{1,4}{p_{2,4}}^2p_{4,u}p_{t,1}p_{x,2} + 4\,c_4m_1p_{1,4}{p_{2,4}}^2p_{4,u}p_{t,2}p_{x,1} + 4\,c_4m_1{p_{2,4}}^3p_{4,u}p_{t,2}p_{x,2}+ \\
4\,c_4m_4{p_{1,4}}^2p_{2,4}p_{4,u}{p_{x,1}}^2 + 8\,c_4m_4p_{1,4}{p_{2,4}}^2p_{4,u}p_{x,1}p_{x,2} + 4\,c_4m_4{p_{2,4}}^3p_{4,u}{p_{x,2}}^2 = 0, \\
. \\
. \\
.
\end{gathered} \tag{16}
$$

By equating the coefficients of each basis term to zero, we derive a system of algebraic constraints on the weights and biases. The resulting solutions, parameterized by these constrained weights and biases, yield the novel exact solutions to the combined Kairat-II-X equation. The effective solutions with weights and biases according to Table 1 are presented in the following Cases.

Table 1: Neural networks architecture for the hyperbolic function solution.

Layer	Neural	Activation function
Input layer	(x,t)	- -
Hidden layer	$(1,2)$	$(\coth(.), \tanh(.))$
Hidden layer	$(3,4)$	$((.), 1/(.))$
Output layer	u	-

Case 1:

$$
\begin{gathered}
c_4 = 0, \quad m_2 = \frac{m_3p_{4,u}}{6p_{2,4}p_{x,2}}, \quad m_4 = -\frac{p_{t,2}\left(2m_3p_{4,u}p_{x,2}^2+3m_0p_{2,4}p_{t,2}+3m_1p_{2,4}p_{x,2}\right)}{3p_{2,4}p_{x,2}^2}, \quad p_{1,3} = p_{2,3} = p_{1,4} = 0, \\
u(x,t) = c_3p_{3,u} + \frac{p_{4,u}}{p_{2,4}\tanh(tp_{t,2}+xp_{x,2}+c_2)} + c_5, \quad p_{2,4}, \quad p_{x,2} \neq 0.
\end{gathered} \tag{17}
$$

Case 2:

$$c_4=0,\quad m_2=\frac{m_3p_{4,u}}{6p_{2,4}p_{x,2}},\quad m_4=-\frac{p_{t,2}\left(2m_3p_{4,u}p_{x,2}^2+3m_0p_{2,4}p_{t,2}+3m_1p_{2,4}p_{x,2}\right)}{3p_{2,4}p_{x,2}^2},\quad p_{1,3}=p_{2,3}=p_{1,4}=0,$$
$$u(x,t)=\begin{cases}\frac{p_{4,u}}{p_{2,4}\tanh(tp_{t,2}+xp_{x,2}+c_2)}+c_5, & p_{3,u}=0,\\ p_{3,u}\left(p_{2,3}\tanh(tp_{t,2}+xp_{x,2}+c_2)+c_3\right)+c_5, & p_{4,u}=0,\quad p_{2,4},\quad p_{x,2}\neq 0.\end{cases}\tag{18}$$

Case 3:

$$c_4=0,\quad m_0=-\frac{p_{x,2}(m_1p_{t,2}+m_4p_{x,2})}{p_{t,2}^2},\quad m_2=m_3=0,\quad p_{1,3}=0,$$
$$u(x,t)=\begin{cases}p_{3,u}\left(p_{2,3}\tanh(tp_{t,2}+xp_{x,2}+c_2)+c_3\right)+\frac{p_{4,u}}{p_{2,4}\tanh(tp_{t,2}+xp_{x,2}+c_2)}+c_5, & p_{1,4}=0,\\ c_3p_{3,u}+\frac{p_{4,u}}{p_{2,4}\tanh(tp_{t,2}+xp_{x,2}+c_2)+p_{1,4}\coth\left(tp_{t,1}+\frac{xp_{t,1}p_{x,2}}{p_{t,2}}+c_1\right)}+c_5, & p_{2,3}=0,\\ p_{x,1}=\frac{p_{t,1}p_{x,2}}{p_{t,2}},\quad p_{t,2}\neq 0.\end{cases}\tag{19}$$

Case 4:

$$c_4=0,\quad m_0=-\frac{p_{x,2}(8m_3p_{4,u}p_{t,2}p_{x,2}+3m_1p_{2,4}p_{t,2}+3m_4p_{2,4}p_{x,2})}{3p_{2,4}p_{t,2}^2},\quad m_2=\frac{m_3p_{4,u}}{6p_{2,4}p_{x,2}},\quad p_{2,3}=\frac{p_{4,u}}{p_{2,4}p_{3,u}},$$
$$p_{1,3}=p_{1,4}=0,\quad u(x,t)=p_{3,u}\left(\frac{p_{4,u}\tanh(tp_{t,2}+xp_{x,2}+c_2)}{p_{2,4}p_{3,u}}+c_3\right)+\frac{p_{4,u}}{p_{2,4}\tanh(tp_{t,2}+xp_{x,2}+c_2)}+c_5,\quad p_{2,4},\quad p_{t,2}\neq 0.\tag{20}$$

Using the following parameters

$$c_2=2,c_3=0.5,c_5=0.5,p_{t,2}=0.5,p_{x,2}=1,p_{2,4}=1,p_{3,u}=1,p_{4,u}=1,\tag{21}$$

we can observe the nonlinear dynamics of the equation, as characterized in Fig 3. Fig 3(a) draws the three-dimensional plot of the time domain $[-10,10]$ and the space domain $[-10,10]$. This waveform exhibits a series of sharp, periodic peaks that rise prominently from the plane, alternating between positive and negative values. The peaks form a consistent pattern that maintains its structure over time. Fig 3(b) presents x-curves at $t=-2,0,2$, visualizing the time evolution of the solution of Eq (20) over time. The waveform shifts to the left with the extension of time. In addition, contour and density plots of Eq (20) are displayed in Fig 3(c) and (d). The diagonal structure in the density plot suggests a steady progression of the waveform as time and space evolve.

Case 5:

$$\begin{gathered}c_4=0,\quad m_0=-\frac{p_{x,1}(2m_3p_{4,u}p_{t,1}p_{x,1}+3m_1p_{1,4}p_{t,1}+3m_4p_{1,4}p_{x,1})}{3p_{1,4}p_{t,1}^2},\quad m_2=\frac{m_3p_{4,u}}{6p_{1,4}p_{x,1}},\\ p_{1,3}=p_{2,3}=p_{2,4}=0,\quad u(x,t)=c_3p_{3,u}+\frac{p_{4,u}}{p_{1,4}\coth(tp_{t,1}+xp_{x,1}+c_1)}+c_5,\quad p_{1,4}\neq 0.\end{gathered}\tag{22}$$

Case 6:

$$c_4=0,\quad m_0=\frac{2\left(p_{1,4}^2-p_{2,4}^2\right)p_{2,4}m_2p_{x,1}^3}{p_{1,4}^2(p_{1,4}p_{t,2}+p_{2,4}p_{t,1})},\quad m_1=\frac{2m_2p_{x,1}^2\left(p_{1,4}^3p_{t,2}-3p_{1,4}^2p_{2,4}p_{t,1}-3p_{1,4}p_{2,4}^2p_{t,2}+p_{2,4}^3p_{t,1}\right)}{p_{1,4}^2(p_{1,4}p_{t,2}+p_{2,4}p_{t,1})},$$
$$m_3=\frac{6m_2p_{x,1}\left(p_{1,4}^2-p_{2,4}^2\right)}{p_{1,4}p_{4,u}},\quad m_4=-\frac{6m_2p_{t,1}p_{x,1}p_{t,2}\left(p_{1,4}^2-p_{2,4}^2\right)}{p_{1,4}(p_{1,4}p_{t,2}+p_{2,4}p_{t,1})},\quad p_{1,3}=p_{2,3}=0,$$
$$p_{x,2}=-\frac{p_{2,4}p_{x,1}}{p_{1,4}},\quad u(x,t)=c_3p_{3,u}+\frac{p_{4,u}}{p_{2,4}\tanh\left(tp_{t,2}-\frac{xp_{2,4}p_{x,1}}{p_{1,4}}+c_2\right)+p_{1,4}\coth(tp_{t,1}+xp_{x,1}+c_1)}+c_5,\quad p_{1,4},\quad p_{2,4}\neq 0.\tag{23}$$

Using the following parameters

$$\begin{gathered}c_1=3,c_2=2,c_3=0.5,c_5=0.5,p_{t,1}=2,p_{t,2}=0.5,p_{x,1}=0.3,p_{x,2}=1,\\ p_{1,4}=1.5,p_{2,4}=1,p_{3,u}=1,p_{4,u}=1,\end{gathered}\tag{24}$$

we can see the nonlinear dynamics of the equation, as characterized in Fig 4. Fig 4(a) draws the three-dimensional plot of the time domain $[-20,20]$ and the space domain $[-50,50]$. Using this values of constants and the associated equation into Eq. (23), the result yields breather-soliton solution as presented in Fig. 4. Fig 4(b) presents x-curves at $t=-2,0,2$, visualizing the time evolution of the solution of Eq (23) over time. The waveform shifts to the left with the extension of time. In addition,

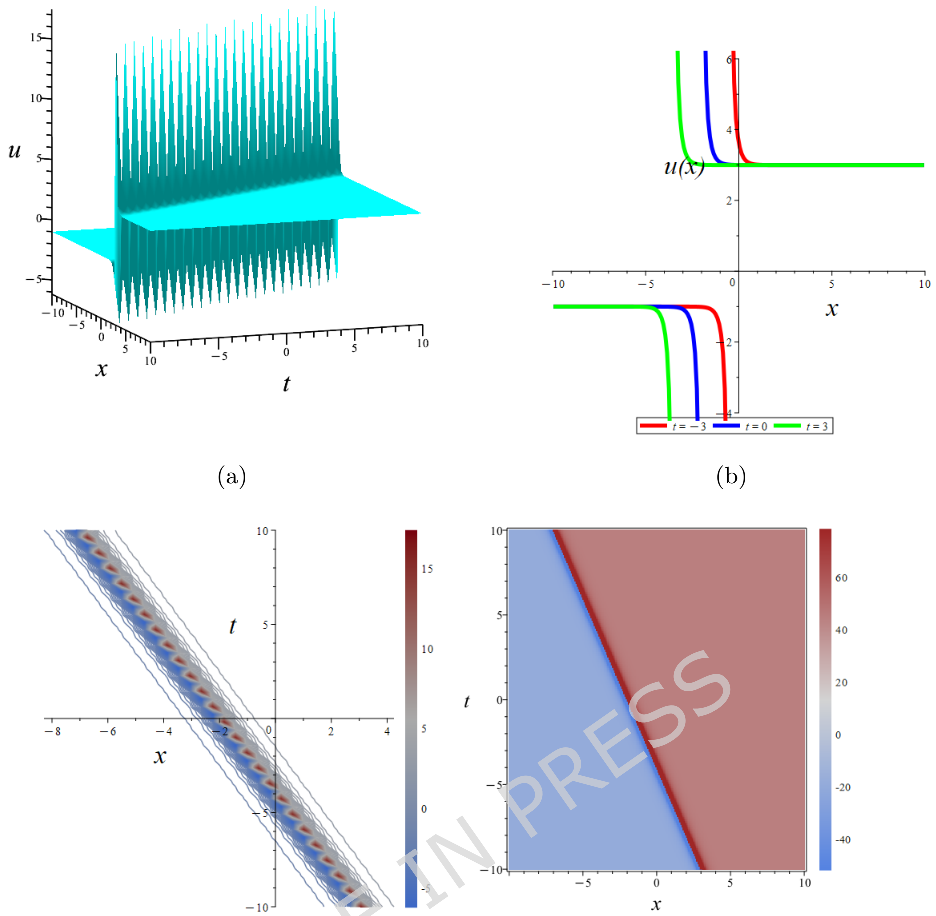

(a) (b)

(c) (d)

Figure 3: Plot of dark-singular soliton solution with parameters in Eq. 20. (a) Three-dimensional plot. (b) Three-dimensional plot. (c) Contour plot (d) Density plot.

contour and density plots of Eq (23) are displayed in Fig 4(c) and (d). The crossover pattern occurs in the positive space and negative time regions.

Case 7:

$$m_4 = -\frac{p_{t,1}\left(4m_2p_{x,1}^3+m_0p_{t,1}+m_1p_{x,1}\right)}{p_{x,1}^2}, \quad c_4 = m_3 = 0, \quad p_{1,3} = p_{2,3} = 0, \quad p_{1,1} = \pm p_{2,4}, \quad p_{t,2} = \mp p_{t,1},$$
$$p_{x,2} = \mp p_{x,1}, \quad u(x,t) = c_3p_{3,u} + \frac{p_{4,u}}{p_{2,4}\tanh(\mp tp_{t,1}\mp xp_{x,1}+c_2)-p_{2,4}\coth(tp_{t,1}+xp_{x,1}+c_1)} + c_5, \quad p_{2,4}, \quad p_{x,1} \neq 0. \tag{25}$$

Case 8:

$$\begin{aligned} m_0 &= -\frac{p_{x,2}(2m_3p_{2,3}p_{3,u}p_{t,2}p_{x,2}+3m_1p_{t,2}+3m_4p_{x,2})}{3p_{t,2}^2}, \quad c_4 = 0, \quad p_{1,3} = p_{2,4} = 0, \quad p_{4,u} = 0, \\ m_2 &= \frac{m_3p_{2,3}p_{3,u}}{6p_{x,2}}, \quad u(x,t) = p_{3,u}\left(p_{2,3}\tanh(tp_{t,2}+xp_{x,2}+c_2)+c_3\right)+c_5, \quad p_{t,2}, \quad p_{x,2} \neq 0. \end{aligned} \tag{26}$$

Remark: In order to confirm the accuracy of this solution, we incorporate the solution (17), (18) (19), (20), (22), (23), (25) and (26) into Eq (3) through the Maple software. The outcome indicates that the left side of the expression equals the right side, indicating that the solution obtained is an exact solution. The solution (17) is the same as the exact solution (3.5) in [90]. We consider the initial and boundary conditions are:

$$\begin{aligned} u(x,0) &= -\frac{12\beta\lambda}{\sqrt{-\lambda}\tau}\coth(2\sqrt{-\lambda}\,x), \\ u(0,t) &= -\frac{12\beta\lambda}{\sqrt{-\lambda}\tau}\coth\left(-\frac{\sqrt{-\lambda}}{\kappa}\left(\sqrt{(16\,\beta\lambda-\alpha)^2-4\,\kappa\rho}+\alpha-16\,\beta\lambda\right)t\right). \end{aligned} \tag{27}$$

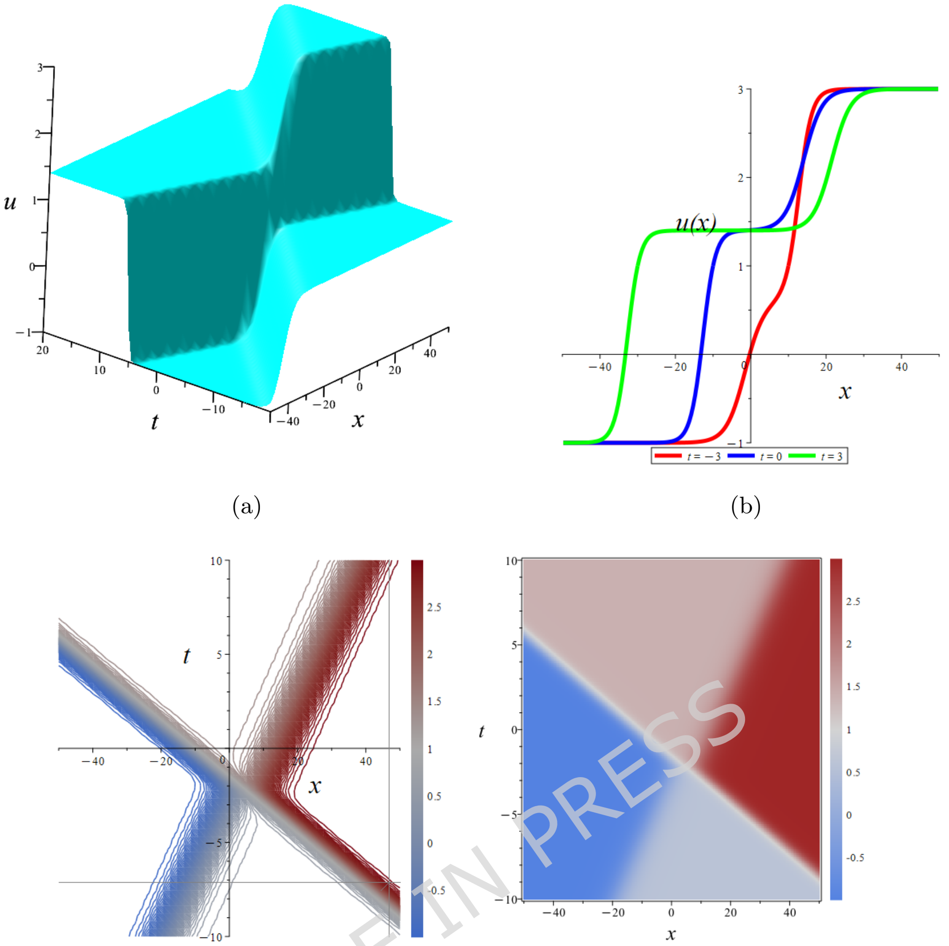

(a) (b)

(c) (d)

Figure 4: Plot of breather-soliton solution solution with parameters in Eq. 23. (a) Three-dimensional plot. (b) Three-dimensional plot. (c) Contour plot (d) Density plot.

By inserting the obtained solution (17) into two constraints of Eq (27), the relevant weight coefficients are obtained as:

$$\begin{aligned} & c_2 = 0, \quad c_5 = -c_3\, p_{3,u}, \quad \frac{p_{4,u}}{p_{2,4}} = 6\,\frac{m_2 p_{x,2}}{m_3}, \quad \frac{p_{4,u}}{p_{2,4}} = -12\,\frac{\beta\,\lambda}{\sqrt{-\lambda}\tau}, \\ & p_{t,2} = \frac{1}{2}\,\frac{\left(-4\,m_2 {p_{x,2}}^2 - m_1 + \sqrt{16\,{m_2}^2 {p_{x,2}}^4 + 8\,m_1 m_2 {p_{x,2}}^2 - 4\,m_0 m_4 + {m_1}^2}\right) p_{x,2}}{m_0} = \\ & -\frac{\sqrt{-\lambda}\left(\sqrt{(16\,\beta\,\lambda - \alpha)^2 - 4\,\kappa\,\rho} + \alpha - 16\,\beta\,\lambda\right)}{\kappa}, \\ & p_{x,2} = 2\,\sqrt{-\lambda}. \end{aligned} \tag{28}$$

So, by putting the weight coefficients back into the exact solution (17), solution (17) under these constraints is obtained as:

$$u(x,t) = -\frac{12\beta\lambda}{\sqrt{-\lambda}\tau}\coth\left(2\,\sqrt{-\lambda}\,x - \frac{\sqrt{-\lambda}}{\kappa}\left(\sqrt{(16\,\beta\lambda - \alpha)^2 - 4\,\kappa\rho} + \alpha - 16\,\beta\lambda\right)t\right), \quad \lambda < 0. \tag{29}$$

3.2. Type 2: Exponential traveling wave solutions

In this subsection, the 2-2-2-1 neural architecture is retained, with changes to the neurons in the hidden layers. The neurons in the first hidden layer both use the exponential function. The second hidden layer contains two neurons, both employing the reciprocal function. The modified architecture configuration is systematically detailed in Table 2. According to the Table 2, the following trial function $u(x,t)$ is expressed as

$$\begin{aligned} & u = p_{3,u}\left(p_{2,3}\mathrm{e}^{tp_{t,2}+xp_{x,2}+c_2} + p_{1,3}\mathrm{e}^{tp_{t,1}+xp_{x,1}+c_1} + c_3\right) + \\ & \frac{p_{4,u}}{p_{2,4}\mathrm{e}^{tp_{t,2}+xp_{x,2}+c_2} + p_{1,4}\mathrm{e}^{tp_{t,1}+xp_{x,1}+c_1} + c_4} + c_5, \quad tp_{t,j} + xp_{x,j} + c_j \neq 0, \quad j = 1, 2. \end{aligned} \tag{30}$$

Substituting Eq. (30) into Eq. (12), we systematically collect like terms with respect to the basis of coefficients and functions. By equating the coefficients of each basis term to zero, we derive a system of algebraic constraints on the weights and biases. The resulting solutions, parameterized by these constrained weights and biases, yield the novel exact solutions to the combined Kairat-II-X equation. The effective solutions with weights and biases according to Table 2 are presented in the following Cases.

Table 2: Neural networks architecture for the hyperbolic function solution.

Layer	Neural	Activation function
Input layer	(x,t)	- -
Hidden layer	$(1,2)$	$(\exp(.),\exp(.))$
Hidden layer	$(3,4)$	$((.),1/(.))$
Output layer	u	-

Case 1:

$$\begin{aligned} &c_4=0,\quad m_0=-\tfrac{p_{x,2}\left(m_2p_{t,2}p_{x,2}^2+m_1p_{t,2}+m_4p_{x,2}\right)}{p_{t,2}^2},\quad m_3=0,\quad p_{1,3}=p_{2,3}=0,\\ &u(x,t)=p_{3,u}\left(p_{2,3}\mathrm{e}^{tp_{t,2}+xp_{x,2}+c_2}+c_3\right)+\tfrac{p_{4,u}}{p_{2,4}\mathrm{e}^{tp_{t,2}+xp_{x,2}+c_2}}+c_5,\quad p_{2,4},\quad p_{t,2}\neq 0. \end{aligned} \tag{31}$$

Case 2:

$$\begin{aligned} &c_4=0,\quad m_0=-\tfrac{p_{x,2}p_{x,1}\left(m_2p_{t,1}p_{t,2}p_{x,1}^2-m_2p_{t,1}p_{t,2}p_{x,2}^2-m_4p_{t,1}p_{x,2}+m_4p_{t,2}p_{x,1}\right)}{p_{t,2}p_{t,1}(p_{t,1}p_{x,2}-p_{t,2}p_{x,1})},\quad m_3=p_{1,4}=0,\\ &m_1=-\tfrac{m_2p_{t,1}^2p_{t,2}p_{x,2}^3-m_2p_{t,1}p_{t,2}^2p_{x,1}^3+m_4p_{t,1}^2p_{x,2}^2-m_4p_{t,2}^2p_{x,1}^2}{p_{t,1}p_{t,2}(p_{t,1}p_{x,2}-p_{t,2}p_{x,1})},\\ &u(x,t)=p_{3,u}\left(p_{2,3}\mathrm{e}^{tp_{t,2}+xp_{x,2}+c_2}+p_{1,3}\mathrm{e}^{tp_{t,1}+xp_{x,1}+c_1}+c_3\right)+\\ &\tfrac{p_{4,u}}{p_{2,4}\mathrm{e}^{tp_{t,2}+xp_{x,2}+c_2}}+c_5,\quad p_{2,4},\quad p_{t,2}p_{t,1}\left(p_{t,1}p_{x,2}-p_{t,2}p_{x,1}\right)\neq 0. \end{aligned} \tag{32}$$

Using the following parameters

$$\begin{aligned} &c_1=0.3,c_2=0.2,c_3=0.5,c_5=0.5,p_{t,1}=0.2,p_{t,2}=0.5,p_{x,1}=0.3,p_{x,2}=0.4,\\ &p_{1,3}=1.5,p_{2,3}=1,p_{3,u}=1,p_{4,u}=1, \end{aligned} \tag{33}$$

we can see the nonlinear dynamics of the equation, as characterized in Fig 5. Fig 5(a) draws the three-dimensional plot of the time domain $[-10,10]$ and the space domain $[-10,10]$. Using this values of constants and the associated equation into Eq. (32), the result yields U soliton solution as presented in Fig. 5. Fig 5(b) presents x-curves at $t=-2,0,2$, visualizing the time evolution of the solution of Eq (32) over time. The waveform shifts to the left with the extension of time. In addition, contour and density plots of Eq (32) are displayed in Fig 5(c) and (d).

Case 3:

$$\begin{aligned} &c_4=0,\quad m_0=-\tfrac{p_{x,2}\left(m_2p_{x,2}^2+m_1\right)}{p_{t,2}},\quad m_3=m_4=p_{1,4}=p_{t,1}=0,\\ &u(x,t)=p_{3,u}\left(p_{2,3}\mathrm{e}^{tp_{t,2}+xp_{x,2}+c_2}+p_{1,3}\mathrm{e}^{xp_{x,1}+c_1}+c_3\right)+\tfrac{p_{4,u}}{p_{2,4}\mathrm{e}^{tp_{t,2}+xp_{x,2}+c_2}}+c_5,\quad p_{2,4},\quad p_{t,2}\neq 0. \end{aligned} \tag{34}$$

Case 4:

$$\begin{aligned} &c_4=0,\quad m_0=-\tfrac{p_{x,2}\left(m_2p_{t,2}p_{x,2}^2+m_1p_{t,2}+m_4p_{x,2}\right)}{p_{t,2}^2},\quad m_3=p_{1,4}=0,\quad p_{t,1}=\pm p_{t,2},\quad p_{x,1}=\pm p_{x,2},\\ &u(x,t)=p_{3,u}\left(p_{2,3}\mathrm{e}^{tp_{t,2}+xp_{x,2}+c_2}+p_{1,3}\mathrm{e}^{\pm tp_{t,2}\pm xp_{x,2}+c_1}+c_3\right)+\tfrac{p_{4,u}}{p_{2,4}\mathrm{e}^{tp_{t,2}+xp_{x,2}+c_2}}+c_5,\quad p_{2,4},\quad p_{t,2}\neq 0. \end{aligned} \tag{35}$$

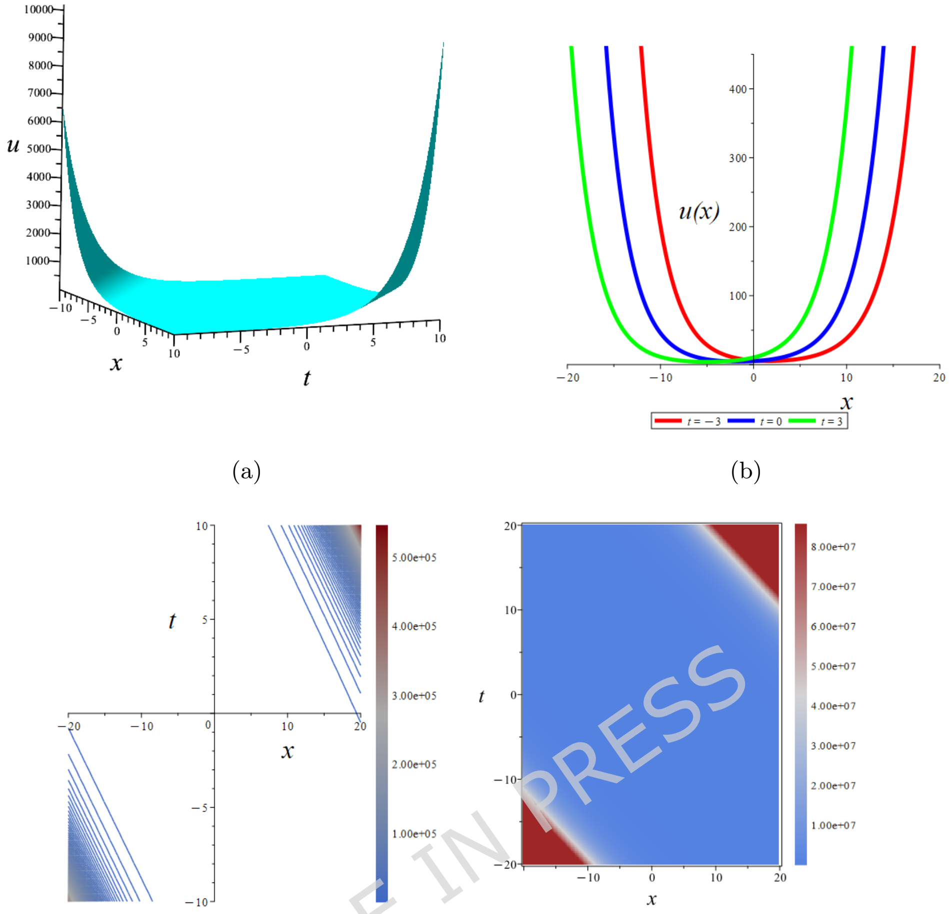

(a) (b)

(c) (d)

Figure 5: Plot of U soliton solution with parameters in Eq. 32. (a) Three-dimensional plot. (b) Three-dimensional plot. (c) Contour plot (d) Density plot.

3.3. Type 3: Periodic-singular wave solutions

In this subsection, the 2-2-2-1 neural architecture is retained, with changes to the neurons in the hidden layers. The neurons in the first hidden layer both use the tan and cot functions. The second hidden layer contains two neurons, both employing the reciprocal function. The modified architecture configuration is systematically detailed in Table 3. According to the Table 3, the following trial function $u(x,t)$ is expressed as

$$\begin{aligned} &u = p_{3,u}\left(p_{2,3}\tan(tp_{t,2}+xp_{x,2}+c_2)+p_{1,3}\cot(tp_{t,1}+xp_{x,1}+c_1)+c_3\right)+ \\ &\frac{p_{4,u}}{p_{2,4}\tan(tp_{t,2}+xp_{x,2}+c_2)+p_{1,4}\cot(tp_{t,1}+xp_{x,1}+c_1)+c_4}+c_5, \quad tp_{t,j}+xp_{x,j}+c_j\neq 0, \quad j=1,2. \end{aligned} \tag{36}$$

Substituting Eq. (36) into Eq. (12), we systematically collect like terms with respect to the basis of coefficients and functions. By equating the coefficients of each basis term to zero, we derive a system of algebraic constraints on the weights and biases. The resulting solutions, parameterized by these constrained weights and biases, yield the novel exact solutions to the combined Kairat-II-X equation. The effective solutions with weights and biases according to Table 3 are presented in the following Cases.

Case 1:

$$\begin{aligned} &c_4=0, \quad m_2=\frac{m_3p_{4,u}}{6p_{2,4}p_{x,2}}, \quad m_4=-\frac{p_{t,2}\left(-2m_3p_{4,u}p_{x,2}^2+3m_0p_{2,4}p_{t,2}+3m_1p_{2,4}p_{x,2}\right)}{3p_{2,4}p_{x,2}^2}, \quad p_{1,3}=p_{2,3}=0, \\ &u(x,t)=c_3p_{3,u}+\frac{p_{4,u}}{p_{2,4}\tan(tp_{t,2}+xp_{x,2}+c_2)}+c_5, \quad p_{2,4}, \ p_{x,2}\neq 0. \end{aligned} \tag{37}$$

Table 3: Neural networks architecture for the hyperbolic function solution.

Layer	Neural	Activation function
Input layer	(x, t)	- -
Hidden layer	$(1, 2)$	$(\cot(.), \tan(.))$
Hidden layer	$(3, 4)$	$((.), 1/(.))$
Output layer	u	-

Case 2:

$$\begin{gathered} c_4 = 0, \quad m_0 = -\frac{p_{x,2}(-8m_3p_{4,u}p_{t,2}p_{x,2}+3m_1p_{2,4}p_{t,2}+3m_4p_{2,4}p_{x,2})}{3p_{2,4}p_{t,2}^2}, \quad m_2 = \frac{m_3p_{4,u}}{6p_{2,4}p_{x,2}}, \quad p_{1,3} = p_{1,4} = 0, \\ p_{2,3} = -\frac{p_{4,u}}{p_{2,4}p_{3,u}}, \quad u(x,t) = p_{3,u}\left(-\frac{p_{4,u}\tan(tp_{t,2}+xp_{x,2}+c_2)}{p_{2,4}p_{3,u}} + c_3\right) + \frac{p_{4,u}}{p_{2,4}\tan(tp_{t,2}+xp_{x,2}+c_2)} + c_5, \quad p_{2,4}, \ p_{t,2} \neq 0. \end{gathered} \tag{38}$$

Using the following parameters

$$c_2 = 0.2, c_3 = 0.5, c_5 = 0.5, p_{t,2} = 0.6, p_{x,2} = 0.5, \quad p_{2,4} = 1.5, p_{3,u} = 1, p_{4,u} = 1, \tag{39}$$

we can see the nonlinear dynamics of the equation, as characterized in Fig 6. Fig 6(a) draws the three-dimensional plot of the time domain $[-5, 5]$ and the space domain $[-5, 5]$. Utilizing these values of constants and the associated equation into Eq. (38), the result yields periodic wave solution as presented in Fig. 6. Fig 6(b) presents x-curves at $t = -2, 0, 2$, visualizing the time evolution of the solution of Eq (38) over time. In addition, contour and density plots of Eq (38) are displayed in Fig 6(c) and (d).

Case 3:

$$\begin{gathered} c_4 = 0, \quad m_0 = -\frac{p_{x,1}(2m_3p_{4,u}p_{t,1}p_{x,1}+3m_1p_{1,4}p_{t,1}+3m_4p_{1,4}p_{x,1})}{3p_{1,4}p_{t,1}^2}, \quad m_2 = -\frac{m_3p_{4,u}}{6p_{1,4}p_{x,1}}, \\ p_{1,3} = p_{2,3} = p_{2,4} = 0, \quad u(x,t) = c_3p_{3,u} + \frac{p_{4,u}}{p_{1,4}\cot(tp_{t,1}+xp_{x,1}+c_1)} + c_5, \quad p_{1,4}, \ p_{t,1} \neq 0. \end{gathered} \tag{40}$$

Case 4:

$$\begin{gathered} c_4 = 0, \quad m_0 = \frac{2\left(p_{1,4}^2-p_{2,4}^2\right)m_2p_{x,1}^3p_{2,4}}{p_{1,4}^2(p_{1,4}p_{t,2}-p_{2,4}p_{t,1})}, \quad m_1 = -\frac{2m_2p_{x,1}^2\left(p_{1,4}^3p_{t,2}+3p_{1,4}^2p_{2,4}p_{t,1}-3p_{1,4}p_{2,4}^2p_{t,2}-p_{2,4}^3p_{t,1}\right)}{p_{1,4}^2(p_{1,4}p_{t,2}-p_{2,4}p_{t,1})}, \\ m_3 = -\frac{6m_2p_{x,1}\left(p_{1,4}^2-p_{2,4}^2\right)}{p_{1,4}p_{4,u}}, \quad m_4 = \frac{6m_2p_{t,1}p_{x,1}p_{t,2}\left(p_{1,4}^2-p_{2,4}^2\right)}{p_{1,4}\left(p_{1,4}p_{t,2}-p_{2,4}p_{t,1}\right)}, \quad p_{1,3} = p_{2,3} = 0, \quad p_{x,2} = \frac{p_{2,4}p_{x,1}}{p_{1,4}}, \\ u(x,t) = c_3p_{3,u} + \frac{p_{4,u}}{p_{2,4}\tan\left(tp_{t,2}+\frac{xp_{2,4}p_{x,1}}{p_{1,4}}+c_2\right)+p_{1,4}\cot(tp_{t,1}+xp_{x,1}+c_1)} + c_5, \quad p_{2,4}, \ p_{1,4}\left(p_{1,4}p_{t,2}-p_{2,4}p_{t,1}\right) \neq 0. \end{gathered} \tag{41}$$

Using the following parameters

$$\begin{gathered} c_1 = 0.5, c_2 = 0.2, c_3 = 0.5, c_5 = 0.5, p_{t,1} = 0.4, p_{t,2} = 0.6, p_{x,1} = 0.4, p_{x,2} = 0.5, \\ p_{2,4} = 1.5, p_{3,u} = 1, p_{4,u} = 1, \end{gathered} \tag{42}$$

we can observe the nonlinear dynamics of the equation, as characterized in Fig 7. Fig 7(a) draws the three-dimensional plot of the time domain $[-5, 5]$ and the space domain $[-5, 5]$. Utilizing these values of constants and the associated equation into Eq. (41), the result yields periodic-breather wave solution as presented in Fig. 7. Fig 7(b) presents x-curves at $t = -2, 0, 2$, visualizing the time evolution of the solution of Eq (41) over time. In addition, contour and density plots of Eq (41) are displayed in Fig 7(c) and (d). The periodic-breather wave moves along the x-axis.

Case 5:

$$\begin{gathered} c_4 = 0, \quad m_0 = -\frac{p_{x,2}\left(2m_3p_{2,3}p_{3,\tan(0.5t+0.6x+1)+1}p_{t,2}p_{x,2}+3m_1p_{t,2}+3m_4p_{x,2}\right)}{3p_{t,2}^2}, \quad m_2 = -\frac{m_3p_{2,3}p_{3,u}}{6p_{x,2}}, \\ p_{1,3} = p_{2,4} = p_{4,u} = 0, \quad u(x,t) = p_{3,u}\left(p_{2,3}\tan(tp_{t,2}+xp_{x,2}+c_2)+c_3\right)+c_5. \end{gathered} \tag{43}$$

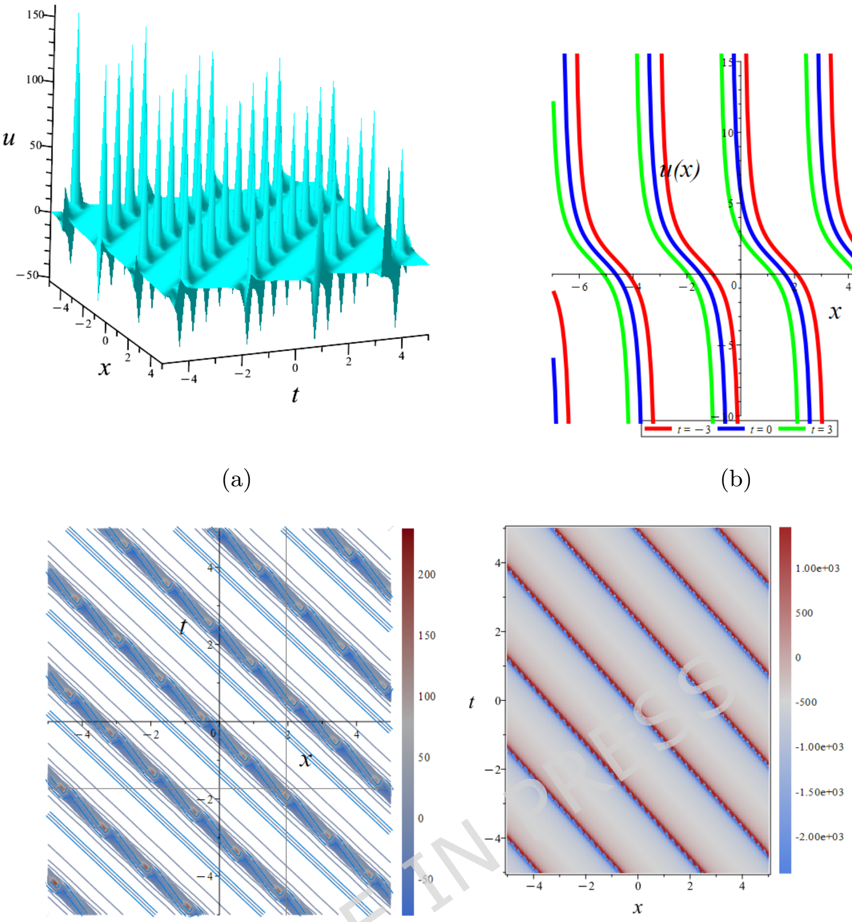

(a) (b)

(c) (d)

Figure 6: Plot of periodic wave solution with parameters in Eq. 38. (a) Three-dimensional plot. (b) Three-dimensional plot. (c) Contour plot (d) Density plot.

Employing the following parameters

$$c_2 = 0.2, c_3 = 0.5, c_5 = 0.5, p_{t,2} = 0.4, p_{t,2} = 0.6, p_{x,2} = 0.5, \quad p_{2,3} = 0.7, p_{3,u} = 1, \tag{44}$$

we can observe the nonlinear dynamics of the equation, as characterized in Fig 8. Fig 8(a) draws the three-dimensional plot of the time domain $[-15, 15]$ and the space domain $[-15, 15]$. Utilizing these values of constants and the associated equation into Eq. (43), the result yields periodic-breather wave solution as presented in Fig. 8. Fig 8(b) presents x-curves at $t = -2, 0, 2$, visualizing the time evolution of the solution of Eq (43) over time. In addition, contour and density plots of Eq (43) are displayed in Fig 8(c) and (d). The periodic wave moves along the x-axis.

3.4. Type 4: Periodic wave solutions

In this subsection, the 2-2-2-1 neural architecture is retained, with changes to the neurons in the hidden layers. The neurons in the first hidden layer both use the sin and cos functions. The second hidden layer contains two neurons, both employing the reciprocal function. The modified architecture configuration is systematically detailed in Table 4. According to the Table 4, the following trial function $u(x, t)$ is expressed as

$$\begin{aligned} u = {} & p_{3,u}\left(p_{1,3}\sin(tp_{t,1} + xp_{x,1} + c_1) + p_{2,3}\cos(tp_{t,2} + xp_{x,2} + c_2) + c_3\right) + \\ & \frac{p_{4,u}}{p_{1,4}\sin(tp_{t,1}+xp_{x,1}+c_1)+p_{2,4}\cos(tp_{t,2}+xp_{x,2}+c_2)+c_4} + c_5, \quad tp_{t,j} + xp_{x,j} + c_j \neq 0, \quad j = 1, 2. \end{aligned} \tag{45}$$

Substituting Eq. (45) into Eq. (12), we systematically collect like terms with respect to the basis of coefficients and functions. By equating the coefficients of each basis term to zero, we derive a system

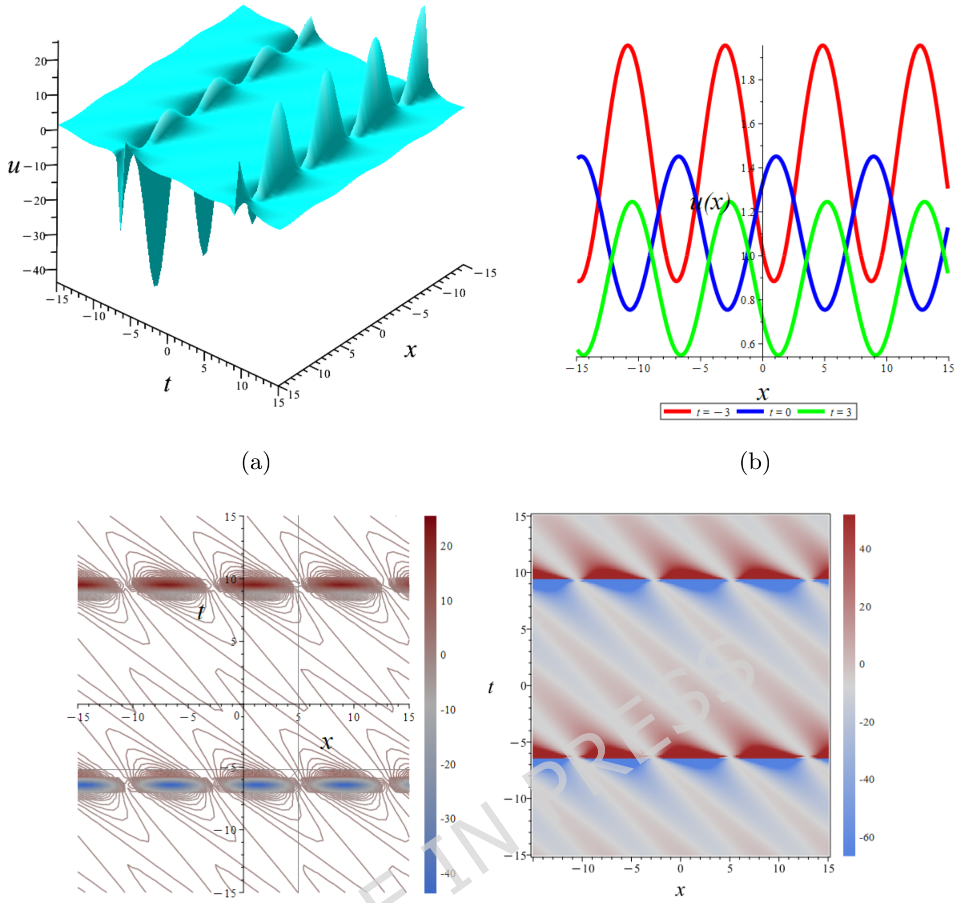

(a) (b)

(c) (d)

Figure 7: Plot of periodic-breather wave solution with parameters in Eq. 41. (a) Three-dimensional plot. (b) Three-dimensional plot. (c) Contour plot (d) Density plot.

of algebraic constraints on the weights and biases. The effective solutions with weights and biases according to Table 4 are presented in the following Cases.

Table 4: Neural networks architecture for the hyperbolic function solution.

Layer	Neural	Activation function
Input layer	(x,t)	- -
Hidden layer	$(1,2)$	$(\sin(.),\cos(.))$
Hidden layer	$(3,4)$	$((.),1/(.))$
Output layer	u	-

Case 1:

$$\begin{aligned} &c_4=0,\quad m_0=-\frac{p_{x,2}(m_1p_{t,2}+m_4p_{x,2})}{p_{t,2}^2},\quad m_2=m_3=0,\quad p_{1,3}=p_{1,4}=p_{x,1}=0,\\ &u(x,t)=p_{3,u}\left(p_{2,3}\cos(tp_{t,2}+xp_{x,2}+c_2)+c_3\right)+\frac{p_{4,u}}{p_{2,4}\cos(tp_{t,2}+xp_{x,2}+c_2)}+c_5,\quad p_{t,2},\ p_{2,4}\neq 0.\end{aligned} \tag{46}$$

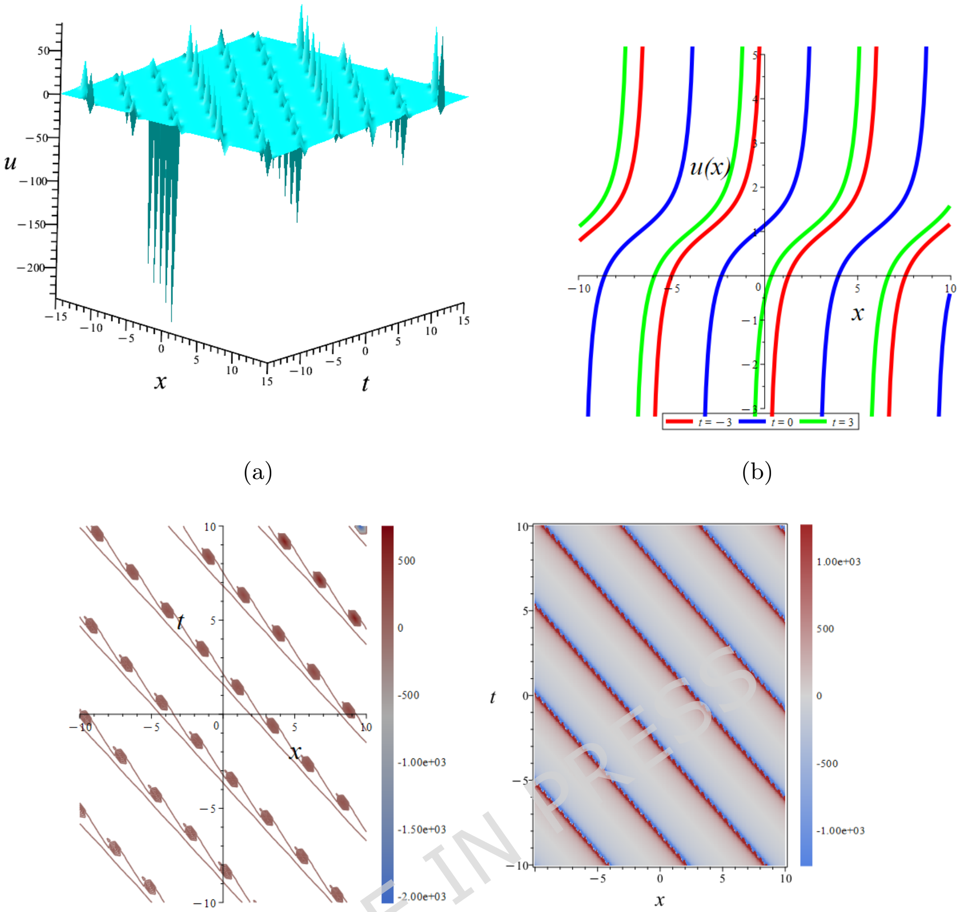

(a) (b)

(c) (d)

Figure 8: Plot of periodic wave solution with parameters in Eq. 43. (a) Three-dimensional plot. (b) Three-dimensional plot. (c) Contour plot (d) Density plot.

Employing the following parameters

$$c_2 = 0.2, c_3 = 0.5, c_5 = 0.5, p_{t,1} = 0.6, p_{t,2} = 0.6, p_{x,2} = 0.5, \quad p_{2,3} = 0.7, p_{2,4} = 1.5, p_{3,u} = 1, p_{4,u} = 1, \tag{47}$$

we can observe the nonlinear dynamics of the equation, as characterized in Fig 9. Fig 9(a) draws the three-dimensional plot of the time domain $[-7, 7]$ and the space domain $[-7, 7]$. Utilizing these values of constants and the associated equation into Eq. (46), the result yields periodic wave solution as presented in Fig. 9. Fig 9(b) presents x-curves at $t = -2, 0, 2$, visualizing the time evolution of the solution of Eq (46) over time. In addition, contour and density plots of Eq (46) are displayed in Fig 9(c) and (d). The periodic wave moves along the x-axis.

Case 2:

$$\begin{aligned} &c_4 = 0, \quad m_4 = -\frac{m_1 p_{t,2}}{p_{x,2}}, \quad m_0 = m_2 = m_3 = 0, \quad p_{1,4} = p_{x,1} = 0, \\ &u(x,t) = p_{3,u}\left(p_{1,3}\sin(tp_{t,1} + c_1) + p_{2,3}\cos(tp_{t,2} + xp_{x,2} + c_2) + c_3\right) + \\ &\frac{p_{4,u}}{p_{2,4}\cos(tp_{t,2} + xp_{x,2} + c_2)} + c_5, \quad p_{x,2}, \ p_{2,4} \neq 0. \end{aligned} \tag{48}$$

Employing the following parameters

$$\begin{aligned} &c_1 = 0.3, c_2 = 0.2, c_3 = 0.5, c_5 = 0.5, p_{t,1} = 0.6, p_{t,2} = 0.6, p_{x,2} = 0.5, \\ &p_{1,3} = p_{2,3} = 0.7, p_{2,4} = 1.5, p_{3,u} = 1, p_{4,u} = 1, \end{aligned} \tag{49}$$

we can observe the nonlinear dynamics of the equation, as characterized in Fig 10. Fig 10(a) draws the three-dimensional plot of the time domain $[-7, 7]$ and the space domain $[-7, 7]$. Utilizing these

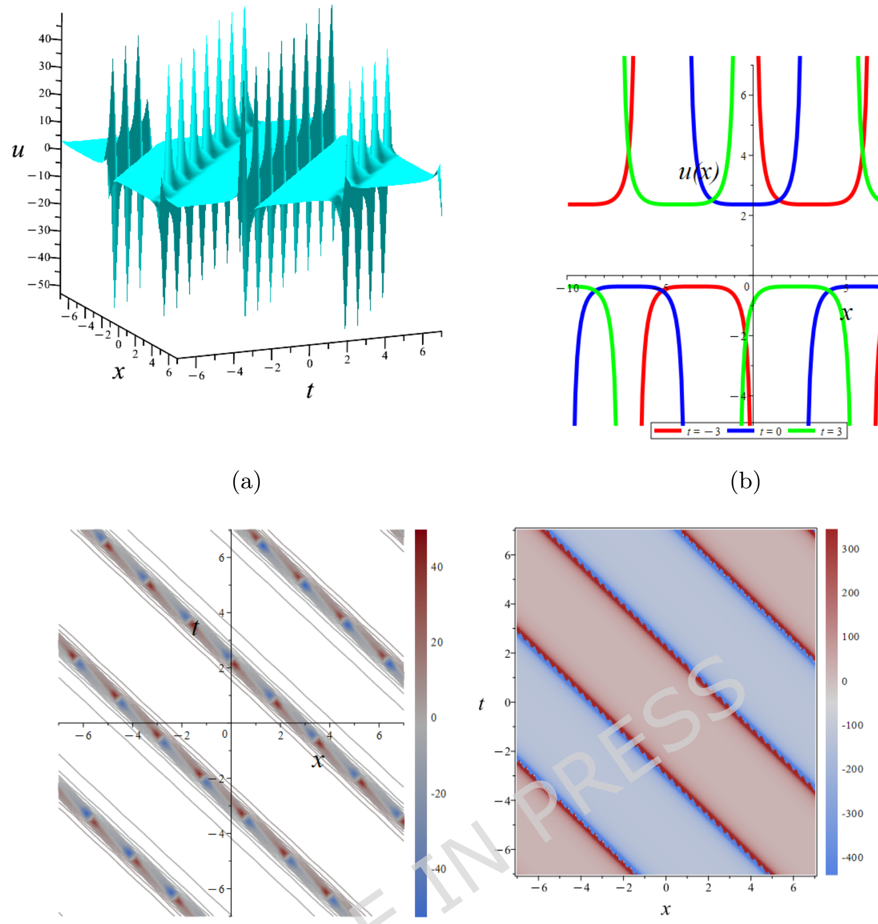

(a) (b)

(c) (d)

Figure 9: Plot of periodic wave solution with parameters in Eq. 46. (a) Three-dimensional plot. (b) Three-dimensional plot. (c) Contour plot (d) Density plot.

values of constants and the associated equation into Eq. (48), the result yields periodic wave solution as presented in Fig. 10. Fig 10(b) presents x-curves at $t = -2, 0, 2$, visualizing the time evolution of the solution of Eq (48) over time. In addition, contour and density plots of Eq (48) are displayed in Fig 10(c) and (d). The breather-periodic wave moves along the $x - t$-axis.

Case 3:

$$\begin{aligned} &c_4 = 0, \quad m_0 = m_3 = 0, \quad m_4 = -\frac{p_{t,2}\left(-m_2 p_{x,2}^2 + m_1\right)}{p_{x,2}}, \quad p_{1,4} = p_{4,u} = p_{x,1} = 0, \\ &u(x,t) = p_{3,u}\left(p_{1,3}\sin(tp_{t,1} + c_1) + p_{2,3}\cos(tp_{t,2} + xp_{x,2} + c_2) + c_3\right) + c_5. \end{aligned} \tag{50}$$

3.5. Type 5: Soliton solutions

In this subsection, the 2-2-2-1 neural architecture is retained, with changes to the neurons in the hidden layers. The neurons in the first hidden layer both use the sinh and cosh functions. The second hidden layer contains two neurons, both employing the reciprocal function. The modified architecture configuration is systematically detailed in Table 5. According to the Table 5, the following trial function $u(x,t)$ is expressed as

$$\begin{aligned} &u = p_{3,u}\left(p_{1,3}\sinh(tp_{t,1} + xp_{x,1} + c_1) + w_{2,3}\cosh(tp_{t,2} + xp_{x,2} + c_2) + c_3\right) + \\ &\frac{p_{4,u}}{p_{1,4}\sinh(tp_{t,1}+xp_{x,1}+c_1)+w_{2,4}\cosh(tp_{t,2}+xp_{x,2}+c_2)+c_4} + c_5, \quad tp_{t,j} + xp_{x,j} + c_j \neq 0, \quad j = 1, 2. \end{aligned} \tag{51}$$

Substituting Eq. (51) into Eq. (12), we systematically collect like terms with respect to the basis of coefficients and functions. By equating the coefficients of each basis term to zero, we derive a system

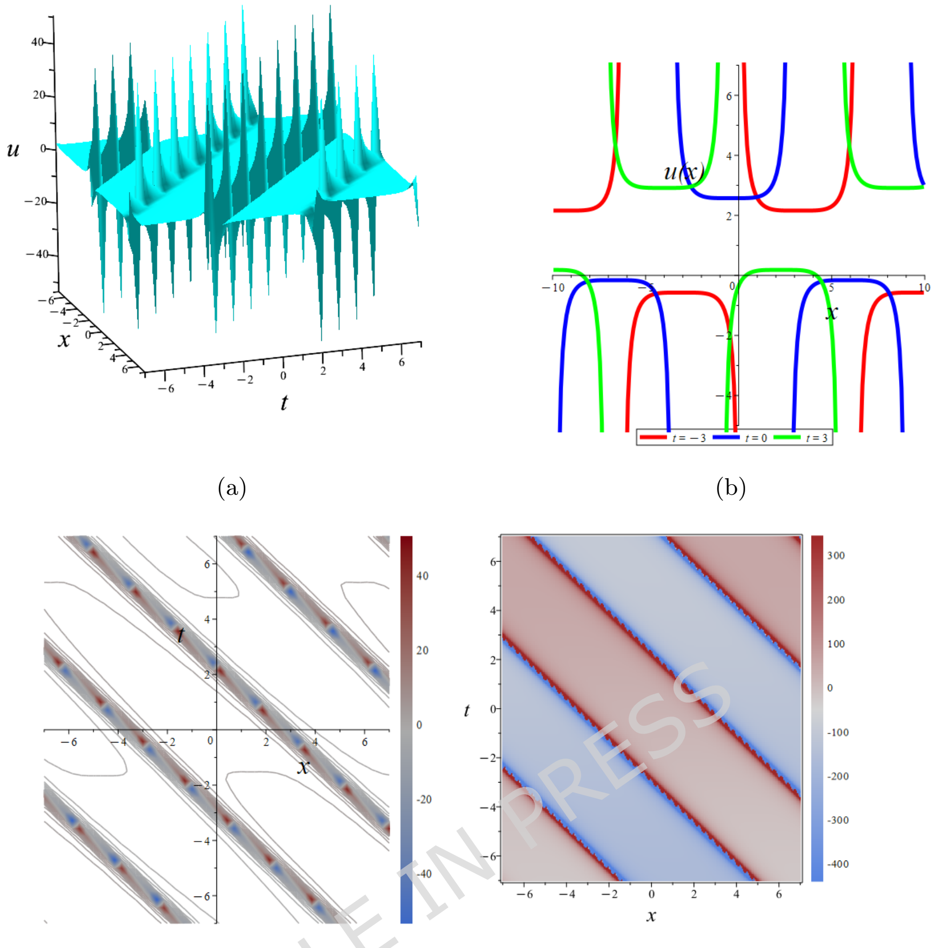

(a) (b)

(c) (d)

Figure 10: Plot of breather-periodic wave solution with parameters in Eq. 48. (a) Three-dimensional plot. (b) Three-dimensional plot. (c) Contour plot (d) Density plot.

Table 5: Neural networks architecture for the hyperbolic function solution.

Layer	Neural	Activation function
Input layer	(x, t)	- -
Hidden layer	$(1, 2)$	$(\sinh(.), \cosh(.))$
Hidden layer	$(3, 4)$	$((.), 1/(.))$
Output layer	u	-

of algebraic constraints on the weights and biases. The effective solutions with weights and biases according to Table 5 are presented in the following Cases.

Case 1:

$$c_4 = 0, \quad m_0 = -\frac{p_{x,2}(m_1 p_{t,2} + m_4 p_{x,2})}{p_{t,2}^2}, \quad m_2 = m_3 = 0, \quad p_{1,4} = 0, \quad p_{x,1} = \frac{p_{t,1} p_{x,2}}{p_{t,2}},$$
$$u(x,t) = p_{3,u}\left(p_{1,3}\sinh\left(tp_{t,1} + \frac{xp_{t,1}p_{x,2}}{p_{t,2}} + c_1\right) + p_{2,3}\cosh(tp_{t,2} + xp_{x,2} + c_2) + c_3\right) + \frac{p_{4,u}}{p_{2,4}\cosh(tp_{t,2} + xp_{x,2} + c_2)} + c_5, \quad p_{t,2},\ p_{2,4} \neq 0. \qquad (52)$$

Employing the following parameters

$$\begin{aligned}&c_1=0.3, c_2=0.2, c_3=0.5, c_5=0.5, p_{t,1}=0.3, p_{t,2}=0.6, p_{x,2}=0.5, \quad p_{1,3}=0.7,\\&p_{2,3}=0.6, p_{2,4}=1.5, p_{3,u}=1, p_{4,u}=1,\end{aligned} \tag{53}$$

we can observe the nonlinear dynamics of the equation, as characterized in Fig 11. Fig 9(a) draws the three-dimensional plot of the time domain $[-10,10]$ and the space domain $[-10,10]$. Utilizing these values of constants and the associated equation into Eq. (52), the result yields soliton solution as presented in Fig. 11. Fig 11(b) presents x-curves at $t=-2,0,2$, visualizing the time evolution of the solution of Eq (52) over time. In addition, contour and density plots of Eq (52) are displayed in Fig 11(c) and (d).

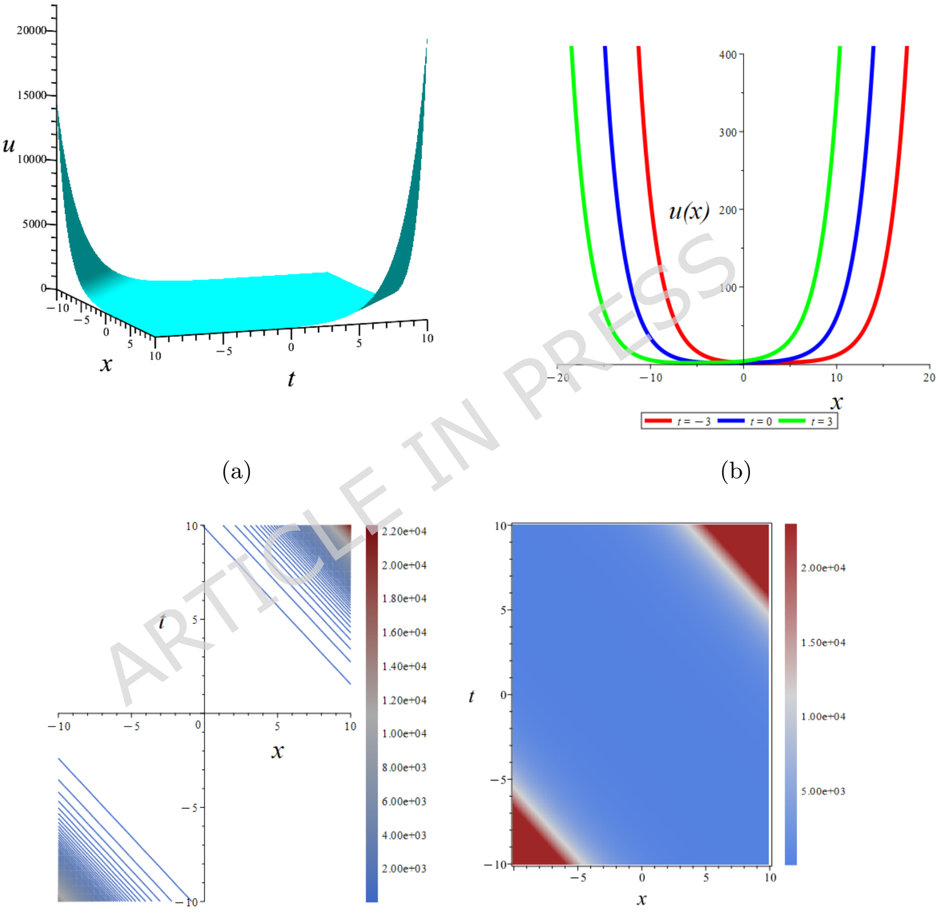

(a) (b)

(c) (d)

Figure 11: Plot of soliton solution with parameters in Eq. 52. (a) Three-dimensional plot. (b) Three-dimensional plot. (c) Contour plot (d) Density plot.

Case 2:

$$\begin{aligned}&c_4=0, \quad m_0=-\frac{p_{x,2}(m_1p_{t,2}+m_4p_{x,2})}{p_{t,2}^2}, \quad m_2=m_3=0, \quad p_{2,3}=0, \quad p_{x,1}=\frac{p_{t,1}p_{x,2}}{p_{t,2}},\\&u(x,t)=p_{3,u}\left(p_{1,3}\sinh\left(tp_{t,1}+\frac{xp_{t,1}p_{x,2}}{p_{t,2}}+c_1\right)+c_3\right)+\\&\frac{p_{4,u}}{p_{1,4}\sinh\left(tp_{t,1}+\frac{xp_{t,1}p_{x,2}}{p_{t,2}}+c_1\right)+p_{2,4}\cosh(tp_{t,2}+xp_{x,2}+c_2)}+c_5, \quad p_{1,4}, \ p_{2,4}\neq 0.\end{aligned} \tag{54}$$

Case 3:

$$
\begin{aligned}
&u(x,t) = p_{3,u}\left(p_{1,3}\sinh(tp_{t,1}+xp_{x,1}+c_1)+p_{2,3}\cosh(tp_{t,2}+xp_{x,2}+c_2)+c_3\right)+\frac{p_{4,u}}{p_{1,4}\sinh(tp_{t,1}+xp_{x,1}+c_1)}+c_5,\\
&u(x,t) = p_{3,u}\left(p_{1,3}\sinh\left(tp_{t,1}+\frac{xp_{t,1}p_{x,2}}{p_{t,2}}+c_1\right)+p_{2,3}\cosh(tp_{t,2}+xp_{x,2}+c_2)+c_3\right)+\\
&\frac{p_{4,u}}{p_{1,4}\sinh\left(tp_{t,1}+\frac{xp_{t,1}p_{x,2}}{p_{t,2}}+c_1\right)}+c_5,\quad p_{t,2},\ p_{1,4}\neq 0.
\end{aligned}
\tag{55}
$$

3.6. Type 6: Soliton-periodic solutions

In this subsection, the 2-2-2-1 neural architecture is retained, with changes to the neurons in the hidden layers. The neurons in the first hidden layer both use the $\sinh, \sin$ and $\cosh, \cos$ functions. The second hidden layer contains two neurons, both employing the reciprocal function. The modified architecture configuration is systematically detailed in Table 6. According to the Table 6, the following trial function $u(x,t)$ is expressed as

$$
\begin{aligned}
&u = p_{3,u}\left(p_{1,3}\sin(tp_{t,1}+xp_{x,1}+c_1)+p_{2,3}\sinh(tp_{t,2}+xp_{x,2}+c_2)+c_3\right)+\\
&\frac{p_{4,u}}{p_{1,4}\cos(tp_{t,1}+xp_{x,1}+c_1)+p_{2,4}\cosh(tp_{t,2}+xp_{x,2}+c_2)+c_4}+c_5,\quad tp_{t,j}+xp_{x,j}+c_j\neq 0,\quad j=1,2.
\end{aligned}
\tag{56}
$$

Substituting Eq. (56) into Eq. (12), we systematically collect like terms with respect to the basis of coefficients and functions. By equating the coefficients of each basis term to zero, we derive a system of algebraic constraints on the weights and biases. The effective solutions with weights and biases according to Table 6 are presented in the following Cases.

Table 6: Neural networks architecture for the hyperbolic function solution.

Layer	Neural	Activation function
Input layer	(x,t)	- -
Hidden layer	$(1,2)$	$(\sin, \sinh(.), \cos, \cosh(.))$
Hidden layer	$(3,4)$	$((.), 1/(.))$
Output layer	u	-

Case 1:

$$
\begin{aligned}
&c_4=0,\quad m_0=-m_1-m_4,\quad m_2=m_3=0,\quad p_{1,3}=p_{1,4}=0,\\
&u(x,t)=p_{3,u}\left(p_{2,3}\sinh(tp_{x,2}+xp_{x,2}+c_2)+x+t+c_3\right)^2+\\
&\frac{p_{4,u}}{(p_{2,4}\cosh(tp_{x,2}+xp_{x,2}+c_2)+x+t)^2}+c_5,\quad p_{2,4}\neq 0.
\end{aligned}
\tag{57}
$$

Employing the following parameters

$$
\begin{aligned}
&c_1=0.3, c_2=0.2, c_3=0.5, c_5=0.5, p_{t,1}=0.3, p_{t,2}=0.6, , p_{x,1}=0.3, p_{x,2}=0.5,\\
&p_{2,3}=0.6, p_{2,4}=1.5, p_{3,u}=1, p_{4,u}=1,
\end{aligned}
\tag{58}
$$

we can observe the nonlinear dynamics of the equation, as characterized in Fig 12. Fig 12(a) draws the three-dimensional plot of the time domain $[-10,10]$ and the space domain $[-10,10]$. Utilizing these values of constants and the associated equation into Eq. (58), the result yields soliton-periodic solution as presented in Fig. 12. Fig 12(b) presents x-curves at $t=-2,0,2$, visualizing the time evolution of the solution of Eq (58) over time. In addition, contour and density plots of Eq (58) are displayed in Fig 12(c) and (d).

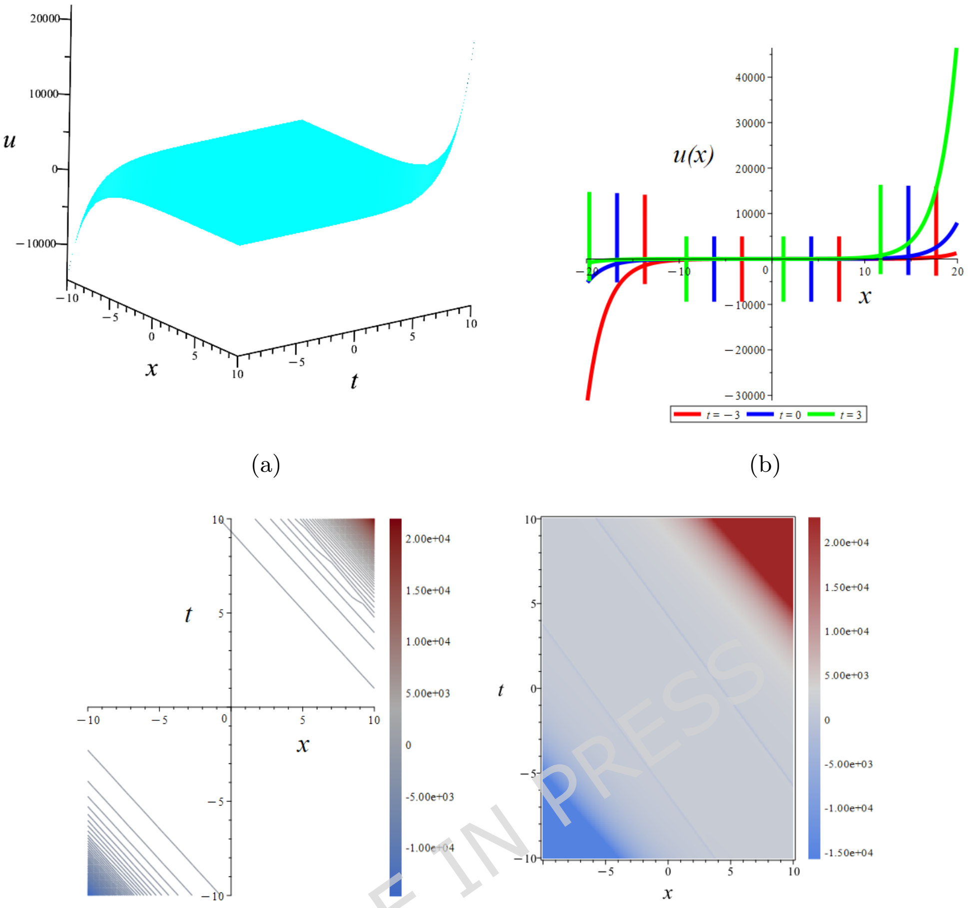

(a) (b)

(c) (d)

Figure 12: Plot of soliton-periodic solution with parameters in Eq. 58. (a) Three-dimensional plot. (b) Three-dimensional plot. (c) Contour plot (d) Density plot.

Case 2:

$$u(x,t)=\begin{cases} p_{3,u}\left(p_{2,3}\sinh(tp_{t,2}+xp_{x,2}+c_2)+c_3\right)+ & \\ \dfrac{p_{4,u}}{p_{1,4}\cos\left(tp_{t,1}+\frac{xp_{t,1}p_{x,2}}{p_{t,2}}+c_1\right)+p_{2,4}\cosh(tp_{t,2}+xp_{x,2}+c_2)}+c_5, & m_0=-\dfrac{p_{x,2}(m_1p_{t,2}+m_4p_{x,2})}{p_{t,2}^2}, \\ p_{3,u}\left(p_{1,3}\sin(tp_{t,1}+xp_{x,1}+c_1)+c_3\right)+\dfrac{p_{4,u}}{p_{1,4}\cos(tp_{t,1}+xp_{x,1}+c_1)}+c_5, & m_0=-\dfrac{p_{x,1}(m_1p_{t,1}+m_4p_{x,1})}{p_{t,1}^2} \\ p_{3,u}\left(p_{1,3}\sin\left(tp_{t,1}+\dfrac{xp_{t,1}p_{x,2}}{p_{t,2}}+c_1\right)+c_3\right)+ & \\ \dfrac{p_{4,u}}{p_{1,4}\cos\left(tp_{t,1}+\frac{xp_{t,1}p_{x,2}}{p_{t,2}}+c_1\right)+p_{2,4}\cosh(tp_{t,2}+xp_{x,2}+c_2)}+c_5, & m_0=-\dfrac{p_{x,2}(m_1p_{t,2}+m_4p_{x,2})}{p_{t,2}^2}, \\ p_{3,u}\left(p_{1,3}\sin\left(tp_{t,1}+\dfrac{xp_{t,1}p_{x,2}}{p_{t,2}}+c_1\right)+p_{2,3}\sinh(tp_{t,2}+xp_{x,2}+c_2)+c_3\right) & \\ +\dfrac{p_{4,u}}{p_{2,4}\cosh(tp_{t,2}+xp_{x,2}+c_2)}+c_5, & m_0=-\dfrac{p_{x,2}(m_1p_{t,2}+m_4p_{x,2})}{p_{t,2}^2}, \\ p_{3,u}\left(p_{1,3}\sin(tp_{t,1}+xp_{x,1}+c_1)+p_{2,3}\sinh(tp_{t,2}+xp_{x,2}+c_2)+c_3\right) & \\ +\dfrac{p_{4,u}}{p_{2,4}\cosh(tp_{t,2}+xp_{x,2}+c_2)}+c_5, & m_0=\dfrac{m_4p_{x,1}p_{x,2}}{p_{t,2}p_{t,1}}, \\ m_1=-\dfrac{m_4(p_{t,1}p_{x,2}+p_{t,2}p_{x,1})}{p_{t,1}p_{t,2}}. & \end{cases} \tag{59}$$

3.7. Type 7: Lump Soliton-periodic solutions

In this subsection, the 2-2-2-1 neural architecture is retained, with changes to the neurons in the hidden layers. The neurons in the first hidden layer both use the $\sinh + x + t$ and $\cosh + x + t$ functions. The second hidden layer contains two neurons, both employing the reciprocal function. The modified architecture configuration is systematically detailed in Table 7. According to the Table 7, the following trial function $u(x,t)$ is expressed as

$$\begin{aligned} &u = p_{3,u}\left(p_{1,3}\sinh(tp_{t,1} + xp_{x,1} + c_1) + p_{2,3}\cosh(tp_{t,2} + xp_{x,2} + c_2) + x + t + c_3\right)^2 + \\ &\frac{p_{4,u}}{\left(p_{1,4}\cosh(tp_{t,1}+xp_{x,1}+c_1)+p_{2,4}\sinh(tp_{t,2}+xp_{x,2}+c_2)+x+t+c_4\right)^2} + c_5, \quad tp_{t,j} + xp_{x,j} + c_j \neq 0, \quad j = 1,2. \end{aligned} \tag{60}$$

Substituting Eq. (60) into Eq. (12), we systematically collect like terms with respect to the basis of coefficients and functions. The effective solutions with weights and biases according to Table 7 are presented in the following Cases.

Table 7: Neural networks architecture for the hyperbolic function solution.

Layer	Neural	Activation function
Input layer	(x,t)	- -
Hidden layer	$(1,2)$	$(\sinh(.) + x + t, \cosh(.) + x + t)$
Hidden layer	$(3,4)$	$((.), 1/(.))$
Output layer	u	-

Case 1:

$$\begin{aligned} &c_4 = 0, \quad m_0 = -m_1 - m_4, \quad m_2 = m_3 = 0, \quad p_{1,3} = p_{1,4} = 0, \\ &u(x,t) = p_{3,u}\left(p_{2,3}\cosh(tp_{x,2} + xp_{x,2} + c_2) + x + t + c_3\right)^2 + \\ &\frac{p_{4,u}}{\left(p_{2,4}\sinh(tp_{x,2}+xp_{x,2}+c_2)+x+t\right)^2} + c_5, \quad p_{2,4} \neq 0. \end{aligned} \tag{61}$$

Case 2:

$$\begin{aligned} &c_4 = 0, \quad m_0 = -m_1 - m_4, \quad m_2 = m_3 = 0, \quad p_{1,3} = p_{2,3} = 0, \\ &u(x,t) = p_{3,u}\left(t + x + c_3\right)^2 + \\ &\frac{p_{4,u}}{\left(p_{1,4}\cosh(tp_{t,1}+xp_{t,1}+c_1)+p_{2,4}\sinh(tp_{x,2}+xp_{x,2}+c_2)+x+t\right)^2} + c_5, \quad p_{1,4}, \quad p_{2,4} \neq 0. \end{aligned} \tag{62}$$

Employing the following parameters

$$\begin{aligned} &c_1 = 0.3, c_2 = 0.2, c_3 = 0.5, c_5 = 0.5, p_{t,1} = 0.3, p_{t,2} = 0.6, , p_{x,1} = 0.3, p_{x,2} = 0.5, \\ &p_{2,3} = 0.6, p_{1,4} = 1, p_{2,4} = 1.5, p_{3,u} = 1, p_{4,u} = 1, \end{aligned} \tag{63}$$

we can see the nonlinear dynamics of the equation, as characterized in Fig 13. Fig 13(a) draws the three-dimensional plot of the time domain $[-10, 10]$ and the space domain $[-10, 10]$. Utilizing these values of constants and the associated equation into Eq. (62), the result yields lump-soliton solution as presented in Fig. 13. Fig 13(b) presents x-curves at $t = -2, 0, 2$, visualizing the time evolution of the solution of Eq (62) over time. In addition, contour and density plots of Eq (62) are displayed in Fig 13(c) and (d).

3.8. Type 8: Lump solutions

In this subsection, the 2-2-2-1 neural architecture is retained, with changes to the neurons in the hidden layers. The neurons in the first hidden layer both use the $x + t$ functions. The second hidden layer contains two neurons, both employing the reciprocal function. The modified architecture

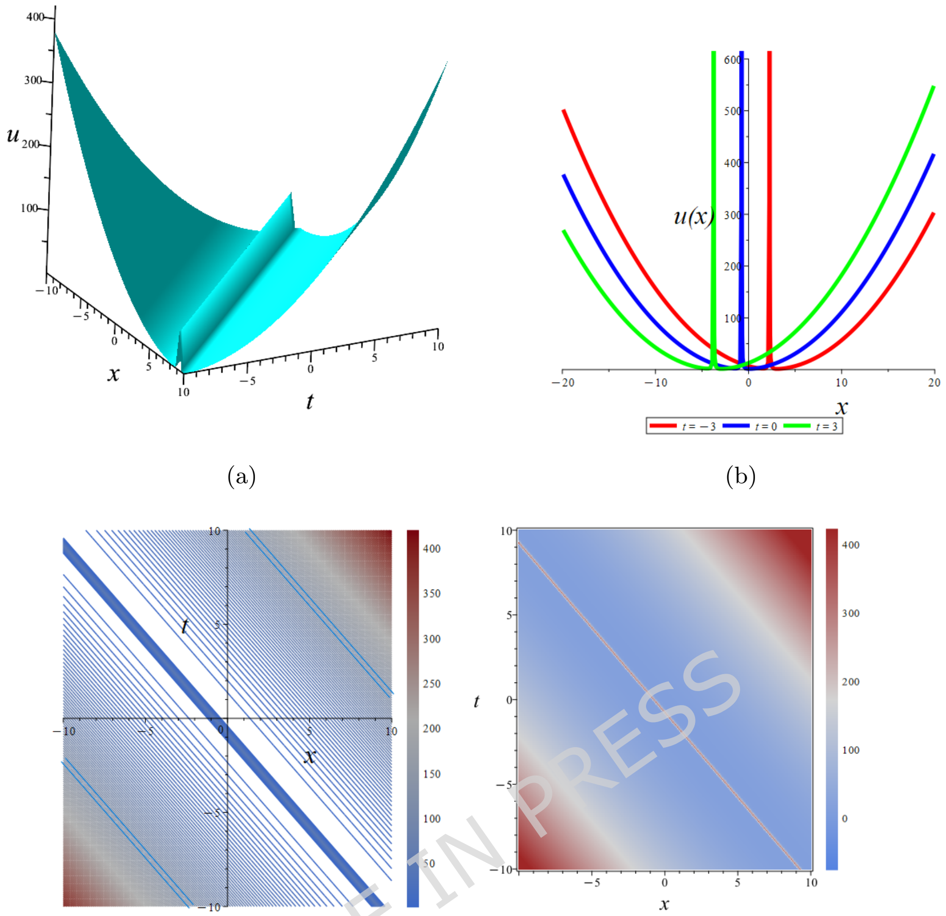

(a) (b)

(c) (d)

Figure 13: Plot of lump-soliton solution with parameters in Eq. 62. (a) Three-dimensional plot. (b) Three-dimensional plot. (c) Contour plot (d) Density plot.

configuration is systematically detailed in Table 8. According to the Table 8, the following trial function $u(x,t)$ is expressed as

$$\begin{aligned} u &= p_{3,u}\left(\left(tp_{t,1}+xp_{x,1}+c_1\right)p_{1,3}+\left(tp_{t,2}+xp_{x,2}+c_2\right)p_{2,3}+c_3\right)^2+ \\ &\frac{p_{4,u}}{\left(\left(tp_{t,1}+xp_{x,1}+c_1\right)p_{1,4}+\left(tp_{t,2}+xp_{x,2}+c_2\right)p_{2,4}+c_4\right)^2}+c_5,\quad tp_{t,j}+xp_{x,j}+c_j\neq 0,\quad j=1,2. \end{aligned} \tag{64}$$

Substituting Eq. (64) into Eq. (12), we systematically collect like terms with respect to the basis of coefficients and functions. The effective solutions with weights and biases according to Table 8 are presented in the following Cases.

Case 1:

$$\begin{aligned} &m_0=-\frac{\left(p_{1,4}p_{x,1}+p_{2,4}p_{x,2}\right)\left(m_1p_{1,4}p_{t,1}+m_1p_{2,4}p_{t,2}+m_4p_{1,4}p_{x,1}+m_4p_{2,4}p_{x,2}\right)}{\left(p_{1,4}p_{t,1}+p_{2,4}p_{t,2}\right)^2},\quad m_2=m_3=0,\quad p_{3,u}=0, \\ &u(x,t)=\frac{p_{4,u}}{\left(\left(tp_{t,1}+xp_{x,1}+c_1\right)p_{1,4}+\left(tp_{t,2}+xp_{x,2}+c_2\right)p_{2,4}+c_4\right)^2}+c_5,\quad p_{1,4},\ p_{2,4}\neq 0. \end{aligned} \tag{65}$$

Case 2:

$$u(x,t)=\begin{cases} \dfrac{p_{4,u}}{\left(\left(-\frac{tp_{2,4}p_{t,2}}{p_{1,4}}-\frac{xp_{2,4}p_{x,2}}{p_{1,4}}+c_1\right)p_{1,4}+\left(tp_{t,2}+xp_{x,2}+c_2\right)p_{2,4}+c_4\right)^2}+c_5, & p_{t,1}=-\dfrac{p_{2,4}p_{t,2}}{p_{1,4}}, \\ p_{x,1}=-\dfrac{p_{2,4}p_{x,2}}{p_{1,4}}, & \\ \dfrac{p_{4,u}}{\left(-\frac{\left(tp_{t,1}+xp_{x,1}+c_1\right)p_{2,4}p_{x,2}}{p_{x,1}}+\left(tp_{t,2}+xp_{x,2}+c_2\right)p_{2,4}+c_4\right)^2}+c_5, & p_{1,4}=-\dfrac{p_{2,4}p_{x,2}}{p_{x,1}}, \\ p_{1,4},\quad p_{x,1}\neq 0. & \end{cases} \tag{66}$$

Table 8: Neural networks architecture for the hyperbolic function solution.

Layer	Neural	Activation function
Input layer	(x,t)	- -
Hidden layer	$(1,2)$	$(x+t, x+t)$
Hidden layer	$(3,4)$	$((.)^2, 1/(.)^2)$
Output layer	u	-

Case 3:

$$
\begin{aligned}
&m_0 = \frac{(m_1p_{1,4}(p_{1,3}p_{t,1}+p_{2,3}p_{t,2})-m_4p_{x,2}(p_{1,3}p_{2,4}-p_{1,4}p_{2,3}))(m_1p_{1,3}(p_{1,4}p_{t,1}+p_{2,4}p_{t,2})+m_4p_{x,2}(p_{1,3}p_{2,4}-p_{1,4}p_{2,3}))}{m_4(2p_{1,3}p_{1,4}p_{t,1}+p_{1,3}p_{2,4}p_{t,2}+p_{1,4}p_{2,3}p_{t,2})^2},\\
&p_{x,1} = -\frac{m_1(p_{1,4}p_{t,1}+p_{2,4}p_{t,2})(p_{1,3}p_{t,1}+p_{2,3}p_{t,2})+m_4p_{x,2}(p_{1,3}p_{2,4}p_{t,1}+p_{1,4}p_{2,3}p_{t,1}+2p_{2,3}p_{2,4}p_{t,2})}{m_4(2p_{1,3}p_{1,4}p_{t,1}+p_{1,3}p_{2,4}p_{t,2}+p_{1,4}p_{2,3}p_{t,2})},\\
&c_4 = -c_1p_{1,4} - c_2p_{2,4},\\
&u(x,t) = p_{3,u}\left((tp_{t,1}+p_{x,1}x+c_1)\,p_{1,3} + (tp_{t,2}+xp_{x,2}+c_2)\,p_{2,3} + c_3\right)^2 + \\
&\frac{p_{4,u}}{((tp_{t,1}+p_{x,1}x+c_1)p_{1,4}+(tp_{t,2}+xp_{x,2}+c_2)p_{2,4}-c_1p_{1,4}-c_2p_{2,4})^2} + c_5,\\
&p_{1,4},\quad p_{2,4},\quad m_4\left(2p_{1,3}p_{1,4}p_{t,1}+p_{1,3}p_{2,4}p_{t,2}+p_{1,4}p_{2,3}p_{t,2}\right) \neq 0.
\end{aligned}
\tag{67}
$$

Employing the following parameters

$$
\begin{aligned}
&c_1 = 0.3, c_2 = 0.2, c_3 = 0.5, c_5 = 0.5, p_{t,1} = 0.3, p_{t,2} = 0.6, , p_{x,1} = 0.3, p_{x,2} = 0.5,\\
&p_{2,3} = 0.6, p_{1,4} = 1, p_{2,4} = 1.5, p_{3,u} = 1, p_{4,u} = 1,
\end{aligned}
\tag{68}
$$

we can see the nonlinear dynamics of the equation, as characterized in Fig 14. Fig 14(a) draws the three-dimensional plot of the time domain $[-3,3]$ and the space domain $[-3,3]$. Utilizing these values of constants and the associated equation into Eq. (62), the result yields lump solution as presented in Fig. 14. Fig 14(b) presents x-curves at $t = -2, 0, 2$, visualizing the time evolution of the solution of Eq (67) over time. In addition, contour and density plots of Eq (67) are displayed in Fig 14(c) and (d).

Case 4:

$$
u(x,t) = \begin{cases}
p_{3,u}\left(\left(\frac{tp_{t,2}p_{x,1}}{p_{x,2}}+p_{x,1}x+c_1\right)p_{1,3} + (tp_{t,2}+xp_{x,2}+c_2)\,p_{2,3}+c_3\right)^2 + \\
\frac{p_{4,u}}{\left(\left(\frac{tp_{t,2}p_{x,1}}{p_{x,2}}+p_{x,1}x+c_1\right)p_{1,4}+(tp_{t,2}+xp_{x,2}+c_2)p_{2,4}-c_1p_{1,4}-c_2p_{2,4}\right)^2} + c_5,\\
p_{t,1} = \frac{p_{t,2}p_{x,1}}{p_{x,2}},\\
m_0 = -\frac{p_{x,2}(m_1p_{t,2}+m_4p_{x,2})}{p_{t,2}^2}, c_4 = -c_1p_{1,4}-c_2p_{2,4},\\
p_{x,1} = -\frac{p_{2,4}p_{x,2}}{p_{1,4}},\\
p_{3,u}\left(\frac{(tp_{t,1}+p_{x,1}x+c_1)p_{1,4}p_{2,3}}{p_{2,4}} + (tp_{t,2}+xp_{x,2}+c_2)\,p_{2,3}+c_3\right)^2 + \\
\frac{p_{4,u}}{((tp_{t,1}+p_{x,1}x+c_1)p_{1,4}+(tp_{t,2}+xp_{x,2}+c_2)p_{2,4}-c_1p_{1,4}-c_2p_{2,4})^2} + c_5,\\
p_{1,3} = \frac{p_{1,4}p_{2,3}}{p_{2,4}},\\
c_4 = -c_1p_{1,4}-c_2p_{2,4},\ m_0 = -\frac{(p_{1,4}p_{x,1}+p_{x,2}p_{2,4})(m_1p_{1,4}p_{t,1}+m_1p_{2,4}p_{t,2}+m_4p_{1,4}p_{x,1}+m_4p_{2,4}p_{x,2})}{(p_{1,4}p_{t,1}+p_{2,4}p_{t,2})^2},\\
p_{3,u}\left((tp_{t,1}+p_{x,1}x+c_1)\,p_{1,3} - \frac{(tp_{t,2}+xp_{x,2}+c_2)p_{1,3}(2p_{1,4}p_{t,1}+p_{2,4}p_{t,2})}{p_{1,4}p_{t,2}} + c_3\right)^2 + \\
\frac{p_{4,u}}{((tp_{t,1}+p_{x,1}x+c_1)p_{1,4}+(tp_{t,2}+xp_{x,2}+c_2)p_{2,4}-c_1p_{1,4}-c_2p_{2,4})^2} + c_5,\\
m_1 = -\frac{2p_{x,2}m_4}{p_{t,2}}, p_{2,3} = -\frac{p_{1,3}(2p_{1,4}p_{t,1}+p_{2,4}p_{t,2})}{p_{1,4}p_{t,2}}, c_4 = -c_1p_{1,4}-c_2p_{2,4},\\
m_0 = \frac{m_4\left(2p_{1,4}^2p_{t,1}p_{x,1}p_{x,2}-p_{1,4}^2p_{t,2}p_{x,1}^2+2p_{1,4}p_{2,4}p_{t,1}p_{x,2}^2+p_{2,4}^2p_{t,2}p_{x,2}^2\right)}{p_{t,2}(p_{1,4}p_{t,1}+p_{2,4}p_{t,2})^2},\quad p_{1,4},\quad p_{2,4} \neq 0.
\end{cases}
\tag{69}
$$

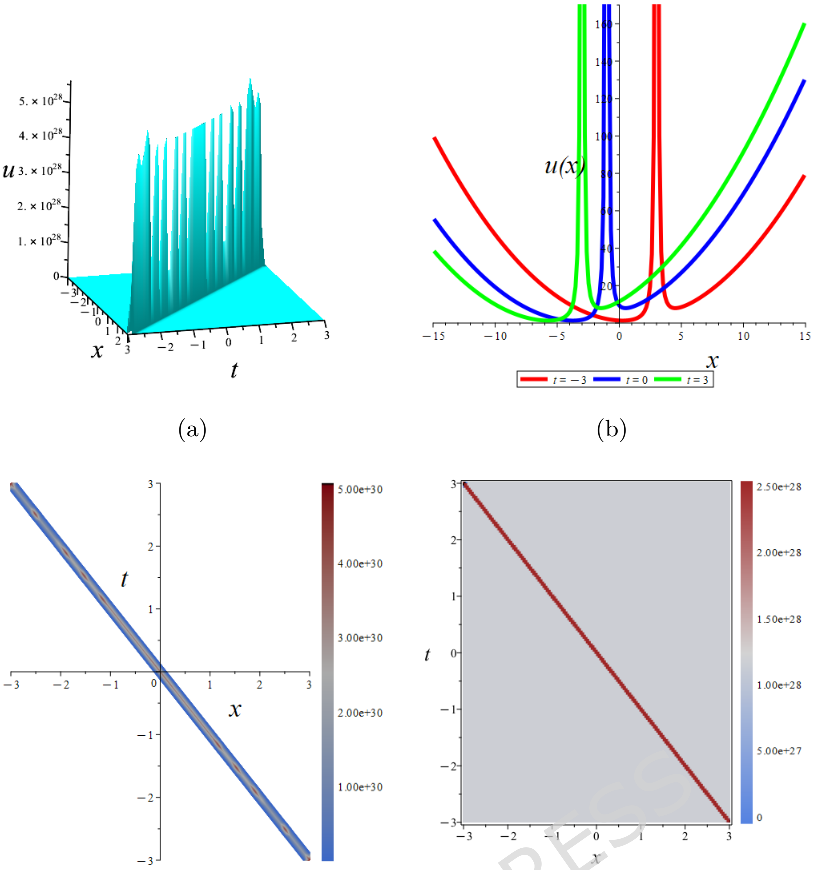

(a) (b)

(c) (d)

Figure 14: Plot of lump solution with parameters in Eq. 67. (a) Three-dimensional plot. (b) Three-dimensional plot. (c) Contour plot (d) Density plot.

Case 5:

$$c_4 = -\frac{p_{1,4}(c_1 m_0 p_{1,3} p_{t,2} + c_2 m_0 p_{2,3} p_{t,2} + c_2 m_1 p_{1,3} p_{x,1} + c_2 m_1 p_{2,3} p_{x,2})}{m_0 p_{1,3} p_{t,2}},\ p_{2,4} = \frac{p_{1,4}(m_0 p_{2,3} p_{t,2} + m_1 p_{1,3} p_{x,1} + m_1 p_{2,3} p_{x,2})}{m_0 p_{1,3} p_{t,2}},$$
$$p_{t,1} = -\frac{m_0 p_{2,3} p_{t,2} + m_1 p_{1,3} p_{x,1} + m_1 p_{2,3} p_{x,2}}{m_0 p_{1,3}},$$
$$u(x,t) = \frac{p_{3,u}\left(\left(t p_{t,1} + x p_{x,1} + c_1\right) p_{1,3} + \left(t p_{t,2} + x p_{x,2} + c_2\right) p_{2,3} + c_3\right)^2 + p_{4,u}}{\left((t p_{t,1} + x p_{x,1} + c_1) p_{1,4} + \frac{\left(t p_{t,2} + x p_{x,2} + c_2\right) p_{1,4}\left(m_0 p_{2,3} p_{t,2} + m_1 p_{1,3} p_{x,1} + m_1 p_{2,3} p_{x,2}\right)}{m_0 p_{1,3} p_{t,2}} + c_4\right)^2} + c_5, \quad m_0 p_{1,3} p_{t,2} \neq 0. \tag{70}$$

Case 6:

$$c_4 = -c_1 p_{1,4} - c_2 p_{2,4}, p_{t,1} = -\frac{p_{2,4} p_{t,2}}{p_{1,4}}, p_{x,1} = -\frac{p_{2,4} p_{x,2}}{p_{1,4}},$$
$$u(x,t) = \frac{p_{3,u}\left(\left(-\frac{t p_{2,4} p_{t,2}}{p_{1,4}} - \frac{x p_{2,4} p_{x,2}}{p_{1,4}} + c_1\right) p_{1,3} + \left(t p_{t,2} + x p_{x,2} + c_2\right) p_{2,3} + c_3\right)^2 + p_{4,u}}{\left(\left(-\frac{t p_{2,4} p_{t,2}}{p_{1,4}} - \frac{x p_{2,4} p_{x,2}}{p_{1,4}} + c_1\right) p_{1,4} + (t p_{t,2} + x p_{x,2} + c_2) p_{2,4} - c_1 p_{1,4} - c_2 p_{2,4}\right)^2} + c_5, \quad p_{1,4} \neq 0. \tag{71}$$

We got so many solution categories that we skipped writing them here.

Comparison of results

A comprehensive analysis of the graphical outcomes for the dark-singular soliton solution of Eq. 20, the breather-soliton solution solution of Eq. 23, U soliton solution of Eq. 32, the periodic wave solution of Eq. 38, the periodic-breather wave solution of Eq. 41, the periodic wave solution of Eq. 43, the periodic wave solution of Eq. 46, the breather-periodic wave solution of Eq. 48, oliton solution of

Eq. 52, the soliton-periodic solution of Eq. 58, the lump-soliton solution of Eq. 62, the lump solution of Eq. 67 are presented in Figs 3-14 to highlight effect of nonlinear wave behaviors.

In [40] new integrable systems was proposed such as Kairat equations and Zhanbhota equation. The Kairat (K) equations can be used in waves analysis in fluid mechanics, and optics. Among the vast spectrum of NLPDEs, the nonlinear K-II and K-X equations and its variants have emerged as paradigmatic models for understanding wave propagation in dispersive nonlinear media [40]. The K equation was studied using multiple analytical approaches, including the Lie point symmetry method [41], the expa function, modified simplest equation and the generalized Kudryashov methods [42], the Riccati modified extended simple equation method [43], the Sardar sub-equation method [44]. Wazwaz et al. [45] proposed a new equation, K-II-X, resulting from combining the equations K-II and K-X. Bifurcation, chaotic behavior, and soliton solutions of the Kairat-II equation via two analytical methods were investigated in [82]. The bifurcation, phase portraits, and exact solutions of the Fokas equation using the improved Cham method were analyzed [83]. The novel Cham method was successfully employed to solve the (2+1)-dimensional Bogoyavlenskii's breaking soliton equations [84]. Several analytical methods have been successfully applied to investigate the combine K-II-X equation, including the generalized (G'/G) method, the generalized projective Riccati equation method [85], the K-II and K-X equations that illustrate relations with the differential geometry of curves and equivalence aspects [86], the K-II and K-X equations in (3+1)-dimensions using new projective Riccati equation approach [87], the K-II-X equation employing the Lie symmetry analysis method [88], the K-II equation and the K-X equation using the (G'/G), and the Bernoulli Sub-ODE, and the modified auxiliary equation methods [89]. We derive various soliton solutions, such as periodic, soliton-periodic, periodic, kink, anti-kink, lump, and lump soliton-periodic solitons. Therefore, the objective of this study is to conduct a comprehensive analytical and dynamical investigation of the combined K-II-X equation by exploiting the neural network-based technique to derive a broad class of exact soliton solutions.

Overall, these results illustrate that the nonlinear model is capable of generating a di verse class of wave phenomena from periodic oscillations and stable solitary waves to exponentially growing or transient pulses by appropriate tuning of the governing parameters. This versatility underscores the model's potential to describe complex physical processes, such as fluid dynamics, optical fiber propagation, and plasma wave dynamics, under different nonlinear regimes.

4. Conclusions

Principal Results: With the rapid development of ML, particularly deep learning, its application to PDEs has gained significant attention. PINNs solves models where purely data-driven models (DDMs) struggle due to scarce data, or where conventional NMs become computationally expensive for complex, high-dimensional PDEs. It leverages the aforementioned concept by embedding PDEs as prior knowledge into neural networks (NNs), training the model by minimizing data loss and physical loss, thereby continuously improving the model's generalization ability and predictive accuracy. This type of method was a DDM that balances data and physics but can only create numerical solutions to the relevant PDEs. PINNs are often categorized as physics-constrained or physics-informed learning rather than strictly unsupervised. The NNs in this study were formulated as an analytical closed-form model rather than a non-transparent black-box model. This methodology uses solely the architectural framework of NNs, omitting the training mechanism entirely. Given that shallow networks exhibit competent function approximation capabilities, our approach minimizes hidden layers and neurons to prevent unnecessary complexity in the explicit model. The exact solution comprises specific basis functions, necessitating deliberate construction of the neural architecture to incorporate these fundamental components. So, the activation function of each neuron must be carefully selected. Especially, these basis functions were often included in the initial and boundary conditions, which greatly simplifies the activation function selection process. However, NNs have better fitting ability and can also be used for the exact solutions. We employed the NN architecture to obtain the exact solutions for combined K-II-X equation.

Comprehensive Result: The comprehensive analysis of the (1+1)-dimensional combined Kairat-II-X differential equation has yielded a rich spectrum of exact analytical solutions, each exhibiting distinct physical characteristics and dynamical behaviors. These comprehensive results demonstrate the remarkable richness and complexity of nonlinear wave dynamics captured by the considered equation. The various solution families reveal different aspects of wave behavior in dispersive nonlinear media, from the robust stability of soliton structures to the complex interaction dynamics of periodic, soliton-periodic, lump waves and the lump-soliton-periodic characteristics of solutions. The interaction scenarios showcase the fundamental principles governing energy and momentum exchange in nonlinear wave systems and lead to dramatic modifications in wave behavior. These findings contribute significantly to our understanding of integrable nonlinear systems and provide valuable insights for applications in fluid dynamics, plasma physics, and nonlinear optics where such wave phenomena play crucial roles in energy transport and system dynamics.

Used Methods: The improved NNs method was used to obtain exact solutions of combined K-II-X equation. Inspired by KANs, the improved NNB method considers activation functions as composites or linear combinations of simple functions. This technique simulates more complex activation functions with fewer parameters. The NNB method and its improved version were utilized the explicit NNs model as the trial function. This model contains weights and biases. By solving the system of equations, the weights and biases were obtained. We employed both methods to obtain exact solutions for the mentioned equations verifying the effectiveness of NNB solutions.

Future Work: This method can also be used to solve other nonlinear models, such as Navier-Stokes equation in fluid dynamics, KdV equation in wave phenomena, Kairat-II and Kairat-X differential equations in the propagation of waves in nonlinear media. Future work will explore these applications and more findings. The physical significance of the extracted solutions is analyzed by presenting various kinds of graphs that illustrate the behavior of the solutions for specific parameter values. Our findings suggest that they may be applied in the future to discover novel and diverse solutions to nonlinear evolution equations that arise in mathematical physics and engineering. The findings in this study can be used to better understand the physical characteristics of different nonlinear complicated models.

Acknowledgment The author would like to acknowledge the Deanship of Graduate Studies and Scientific Research, Taif University for funding this work.

Funding: Training Program for Young and Middle aged Research Backbone Teachers of Wenshan University, No. 2023GG06.

Fund Project of Yunnan Provincial Department of Education, No. 2025J1009.

Availability of Data and Materials: The datasets generated during and/or analyzed during the current study are available from the corresponding author on reasonable request.

Competing interests: The authors declare they have no competing interests regarding the publication of the article.

Authors' Contribution: Conceptualization, P.Z. and K.H.M.; Methodology, J.M., M.L. and O.A.I.; Software, N.J.B. and R.N.; Investigation, A.A.F.; Resources, N.J.B. and N.N.; Writing-original draft, P.Z., J.M., M.L., O.A.I., N.J.B., A.A.F., K.H.M., R.N. and N.N.; Supervision, N.J.B. All authors have read and agreed to the published version of the manuscript.

References

References

[1] Yu, W., Wang, P., Zhao, M., Qu, Y. & Du, X. Fluid-structure interaction simulation of floating structure interacting with the combined effect of wave-current-earthquake based on CFD method. *Ocean Eng.* **339**, 122192 (2025).

[2] Gao, H., Liu, T., Chen, X., Zeng, H., Jiang, J., Wang, X. & Khoo, B. C.Turbulence correlation between moving trains and anemometer towers: Theoretical analysis, field measurements and simulation. *J. Wind Eng. Indus. Aerodyn.* **255**, 105949 (2024).

[3] Zhang, Q., Li, J., Lu, H., Zou, H., Li, K., Liang, Y. & Liu, J. framework with CPU-GPU architecture for high-fidelity real-time urban wind field simulation. *Building Environment* **283**, 113313 (2025).

[4] Liu, M., Mei, S., Liu, P., Gasimov, Y., & Cattani, C. A new x-ray medical-image-enhancement method based on multiscale shannon-cosine wavelet. *Entropy* **24**(12), 1754 (2022).

[5] Ali, N.H., Mohammed, S.A. & Manafian, J. New explicit soliton and other solutions of the Van der Waals model through the ESHGEEM and the IEEM. *J. Modern Tech. Eng.* **8**(1), 5-18 (2023).

[6] Dehghan, M. & Manafian, J. The solution of the variable coefficients fourth-order parabolic partial differential equations by homotopy perturbation method. *Z. Naturforschung A* **64a**, 420-430 (2009).

[7] Shen, X. et al. Abundant wave solutions for generalized Hietarinta equation with Hirota's bilinear operator. *Modern Phys. Lett. B* **36**(10), 2250032 (2022).

[8] Ren, K., Miao, J., Qing, H., Xu, W., Zhang, X., He, Z. & Lu, F. Probing to dynamics of a tube-core sandwich enhanced liquid-filled tank subjected to hydrodynamic ram. *Thin Walled Struct.* **215**, 113573 (2025).

[9] Yuan, G., Song, J., Yang, Y., Ni, B., Yang, D. & Xue, Y. Experimental study on icebreaking mechanism and failure modes of submerged high-pressure water jets. *Ocean Eng.* **323**, 120586 (2025).

[10] Yuan, G., Wang, X., Ni, B., Xu, W., Yang, D. & Xue, Y. Experimental study on load characteristic and icebreaking process of submerged Venturi cavitating water jets. *J. Fluids Struct.* **137**, 104374 (2025).

[11] Lakestani, M. & Manafian, J. Analytical treatments of the space-time fractional coupled nonlinear Schrödinger equations. *Opt. Quant. Elec.* **50**, 396 (2018).

[12] Dehghan, M., Manafian, J. & Saadatmandi, A. Solving nonlinear fractional partial differential equations using the homo- topy analysis method. *Num. Meth. Partial Diff. Eq J.* **26**, 448-479 (2010).

[13] Li, Y., Rui, Z., & Hu, B. Monotone iterative and quasilinearization method for a nonlinear integral impulsive differential equation. *AIMS Math.* **10**(1), 21-37 (2025).

[14] Gintautas, V. Resonant forcing of nonlinear systems of differential equations. *Chaos* **18**(3), 033118 (2008).

[15] Wazwaz, A.M. Solitons and singular solitons for a variety of Boussinesq-like equations. *Ocean Eng.* **53**, 1-5 (2012).

[16] Ma, C., et al. High-efficiency topology optimization method for thermal-fluid problems in cooling jacket of high-speed motorized spindle. *Int. Commun. Heat Mass Trans.* **169**(A), 109533 (2025).

[17] Bo, Y., Tian, D., Liu, X. & Jin, Y. Discrete Maximum Principle and Energy Stability of the Compact Difference Scheme for Two-Dimensional Allen-Cahn Equation. *J. Function Spaces* **2022**(1), 8522231 (2022).

[18] Yuan, G., Ni, B., Liu, P. & Kim, D. K. Ice damage characteristics under high pressure water jet based on Johnson-Holmquist II brittle constitutive model. *Phys. Fluids* **37**(8), 86153 (2025).

[19] Alam, N., et al. Bifurcation analysis, chaotic behaviors, and explicit solutions for a fractional two-mode Nizhnik-Novikov-Veselov equation in mathematical physics. *AIMS Math.* **10**(3), 4558-4578 (2025).

[20] Yue, T. Some results on the nonuniform polynomial dichotomy of discrete evolution families. *Hiroshima Math. J.* **55**(2), 183-201 (2025).

[21] Zhang, H.H., Fan, Z.H. & Chen, R.S. Marching-on-in-degree solver of time-domain finite element boundary integral method for transient electromagnetic analysis. *IEEE Trans. Anten. Prop.* **62**(1), 319-326 (2013).

[22] Zhang, H.H., Sha, W.E.I. & Jiang, L.J. Fast monostatic scattering analysis based on Bayesian compres sive sensing. *Int. Appl. Comput. Elect. Soc. Symposium-Italy (ACES)* 26-30 (2017).

[23] Dehghan, M., Manafian, J. & Saadatmandi, A. The solution of the linear fractional partial differential equations using the homotopy analysis method. *Z. Naturfors. A* **65**(11), 935 (2010).

[24] Ren, F., Zhuang, P., Chen, X., Yu, H. & Yang, H. Physics-Informed Extreme Learning Machine (PIELM) for Stefan problems. *Comput. Meth. Appl. Mech. Eng.* **441**, 118015 (2025).

[25] Ablowitz, M.J. & Clarkson, P.A. Solitons, nonlinear evolution equations and inverse scattering. *Cambridge University Press* (2021).

[26] Zhang, M., et al. Characteristics of the new multiple rogue wave solutions to the fractional generalized CBS-BK equation. *J. Adv. Res.* **38**, 131-142 (2022).

[27] Manafian, J., Mohammadi-Ivatlo, B. & Abapour, M. Breather wave, periodic, and cross-kink solutions to the generalized Bogoyavlensky-Konopelchenko equation. *Math. Meth. Appl. Sci.* **43**(4), 1753-1774 (2020).

[28] Qian, Y., et al. Multiple-order line rogue wave, lump and its interaction, periodic, and cross-kink solutions for the generalized CHKP equation. *Propuls. Power Res.* **10**, 277-293 (2021).

[29] Ma, W. X. N-soliton solutions and the Hirota conditions in (1+1)-dimensions. *Int. J. Nonlinear Sci. Numer. Simul.* **23**, 123-133 (2022).

[30] Nan, T. et al. Generalized Trial Equation Scheme and Enhance Modified Extended Tanh Function Method with Nonparaxial Pulse Propagation to the Cubic-Quintic Nonlinear Helmholtz Equation. *Qualit. Theo. Dyn. Sys.* **24**, 183 (2025).

[31] Zhu, H. et al. Conservation law, Chupin Liu's theorem and propagation of pulses in optical metamaterials modeled by NLSE with power law nonlinearity. *Sci. Reports* **15**, 21649 (2025).

[32] Tariq, K.U. et al. On the structure of the higher dimensional Date-Jimbo-Kashiwara-Miwa model emerging in water waves. *Discover Appl. Sci.* **7**, 576 (2025).

[33] Ahmed, A., Alharbi, T.G., Alharbi, A.R. & Hashim, I. Traveling wave reductions and adaptive moving mesh computations for the improved Boussinesq equation. *AIMS Math.* **10**(12), 28374-28395 (2025).

[34] Guo, S., Kong, D., Manafian, J., Mahmoud, K. H., Alsubaie, A. S. A., Kumari, N. & Ahmad, N. Modulational stability and multiple rogue wave solutions for a generalized (3+1)-D nonlinear wave equation in fluid with gas bubbles. *Alex. Eng. J.* **106**, 1-18 (2024).

[35] Hong, X., et al. Multiple soliton solutions of the generalized Hirota-Satsuma-Ito equation arising in shallow water wave. *J. Geom. Phys.* **170**, 104338 (2021).

[36] Aghazadeh, A. & Lakestani, M. Application of cubic B-splines for second order fractional Sturm-Liouville problems. *Math. Comput. Simul.* **238**, 479-496 (2025).

[37] Aghazadeh, A. & Lakestani, M. Constructing optical soliton wave structure and modulation instability analysis for coupled fractional Lakshmanan-Porsezian-Daniel equation with Kerr's law nonlinearity. *Sci. Reports* **15**, 45294 (2025).

[38] Rao, X., Manafian, J., Mahmoud, K.H., Hajar, A., A. B. Mahdi, A.B. & Zaidi, M. The nonlinear vibration and dispersive wave systems with extended homoclinic breather wave solutions. *Open Phys.* **20**, 795-821 (2022).

[39] Gasimov, Y., Manafian, J. & Aliyeva, A. New approach of (G'/G)-expansion method to solve the fractional differential equations arising in fluid mechanics. *J. Contemp. Appl. Math* **15**, 124-141 (2025).

[40] Myrzakulova, Zh, et al. Integrability, geometry and wave solutions of some Kairat equations. *arXiv preprint arXiv* **2307**, 00027 (2023).

[41] Faridi, W.A., et al. The Lie point symmetry criteria and formation of exact analytical solutions for Kairat-II equation: Paul-Painleve approach. *Chaos Solitons Frac.* **182**, 114745 (2024).

[42] Awadalla, M., et al. The analytical solutions to the M-fractional Kairat-II and Kairat-X equations. *Front. Phys.* **11**, 1335423 (2023).

[43] Xiao, Y., et al. Exploring the dynamical behaviourofoptical solitons in integrable kairat II and kairat-X equations *Phys. Scr.* **99**(9), 095261 (2024).

[44] Aldwoah, K., et al. Exploring the impact of Brownian motion on novel closed-form solutions of the extended Kairat-II equation. *PloS one* **20**(1), e0314849 (2025).

[45] Wazwaz, A.M., Alhejaili, W. & El-Tantawy, S. Study of a combined Kairat II-X equation: Painleve integrability, multiple kink, lump and other physical solutions. *Int. J. Num. Meth. Heat Fluid Flow* **34**(10), 3715-3730 (2024).

[46] Hirota, R. The Direct Method in Soliton Theory, *Cambridge University Press, New York,* (2004).

[47] Xu, Y., et al. Conservation law, stability analysis, degenerate lump and traveling wave solutions for (2+1)-dimensional KP-BBM equation. *Qualit. Theo. Dyn. Sys.* **24**, 246 (2025).

[48] Q. Zou, et al. Exact breather waves solutions in a spatial symmetric nonlinear dispersive wave model in (2+1)-dimensions. *Sci. Reports* **14**, 31718 (2024).

[49] Manafian, J., Murad, M.A.S., Alizadeh, A. & Jafarmadar, S. M-lump, interaction between lumps and stripe solitons solutions to the (2+1)-dimensional KP-BBM equation. *Eur. Phys. J. Plus* 135, 167 (2020).

[50] Pan, Y., Manafian, J., Zeynalli, S.M., Al-Obaidi, R., Sivaraman, R. & Kadi, A. N-Lump solutions to a (3+1)-dimensional variable-coefficient generalized nonlinear wave equation in a liquid with gas bubbles. *Qual. Theo. Dyn. Sys.* **21**, 127 (2022).

[51] Dawod, L.A., Lakestani, M. & Manafian, J. Breather wave solutions for the (3+1)-D generalized shallow water wave equation with variable coefficients. *Qualit. Theo. Dyn. Sys.* **22**, 127 (2023).

[52] Ilhan, O.A., Manafian, J. & Shahriari, M. Lump wave solutions and the interaction phenomenon for a variable-coefficient Kadomtsev-Petviashvili equation. *Comput. Math. Appl.* **78**(8), 2429-2448 (2019).

[53] Ma, W.X. & Zhou, Y. Lump solutions to nonlinear partial differential equations via Hirota bilinear forms. *J. Diff. Eq.* **264**(4) 2633-2659 (2018).

[54] Ding, L., Ma, W.X., Chen, Q. & Huang, Y. Lump solutions of a nonlinear PDE containing a third-order derivative of time. *Appl. Math. Let.* **112**, 106809 (2021).

[55] Seadawy, A.R., Rizvi, S.T.R. & Zahed, H. Lump-type solutions, lump solutions, and mixed rogue waves for coupled nonlinear generalized Zakharov equations. *Math.* **11**(13) 2856 (2023).

[56] Batwa, S. & Ma, W.X. Lump solutions to a generalized Hietarinta-type equation via symbolic computation. *Front. Math. China* **15**, 435-450 (2020).

[57] Lu, J., Bilige, S., Gao, X., Bai, Y. & Zhang, R. Abundant Lump Solutions and Interaction Phenom ena to the Kadomtsev-Petviashvili-Benjamin-Bona-Mahony Equation. *J. Appl. Math. Phys.* **6**(8), 1733-1747 (2018).

[58] He L. & Zhao, Z. Multiple lump solutions and dynamics of the generalized (3+1)-dimensional KP equation. *Modern Phys. Let. B* **34**(15), 2050167 (2020).

[59] Manafian, J., Lakestani, M. N-lump and interaction solutions of localized waves to the (2+1)-dimensional variable-coefficient Caudrey Dodd Gibbon Kotera Sawada equation. *J. Geom. Phys.* **150**, 103598 (2020).

[60] Wen, G.G., Li, Z.Y., Azizzadenesheli, K., Anandkumar, A. & Benson, S.M. U-fno-an enhanced fourier neural operator-based deep-learning model for flow. *Adv. Water Resources* **163**, 104180 (2022).

[61] Mustafa, N., Rahman, J.U. & Omame, A. Modelling of Marburg virus transmission dynamics: a deep learning-driven approach with the effect of quarantine and health awareness interventions. *Model. Earth Sys. Environ.* **10**, 7337-7357 (2024).

[62] Raissi, M., Perdikaris, P. & Karniadakis, G.E. Physics-informed neural networks: A deep learning framework for solving forward and inverse problems involving nonlinear partial differential equations. *J. Comput. Phys.* **378**, 686-707 (2019).

[63] Xiang, Z.X., Peng, W., Liu, X. & Yao, W. Self-adaptive loss balanced Physics-informed neural networks. *Neurocomput.* **496**, 11-34 (2022).

[64] Anagnostopoulos, S.J., Toscano, J.D., Stergiopulos, N. & Karniadakis, G.E. Residual-based attention in physics-informed neural networks. *Comput. Meth. Appl. Mech. Eng.* **421**, 116805 (2024).

[65] Liu, Z., et al. Kan: Kolmogorov-arnold networks. (2024).

[66] Zhang, R.F. & Bilige, S. Bilinear neural network method to obtain the exact analytical solutions of nonlinear partial differential equations and its application to p-gbkp equation. *Nonlinear Dyn.* **95**(4), 3041-3048 (2019).

[67] Zhang, R.F. & Li, M.C. Bilinear residual network method for solving the exactly explicit solutions of nonlinear evolution equations. *Nonlinear Dyn.* **108**(1), 521-531 (2022).

[68] Zhang, Y., Zhang, R.F. & Yuen, K.V. Neural network-based analytical solver for fokker-planck equation. *Eng. Appl. Artif. Intel.* **125**, 106721 (2023).

[69] Xie, X.R. & Zhang, R.F. Network-based symbolic calculation approach for solving the Korteweg-de Vries equation. *Chaos Solitons Frac.* **194**, 116232 (2025).

[70] Wang, J.W., et al. Fractional sub-equation neural networks (fSENNs) method for exact solutions of space-time fractional partial differential equations. *Chaos: An Interdiscip. J. Nonlinear Sci.* **35**(4), 043110 (2025).

[71] Liu, Y.Q., Yuan, S.H., Zhang, R.F., Yan, L.M., Dong, H.Y. & Feng, L.B. A novel (G'/G)-expansion neural networks method for exactly explicit solutions of nonlinear partial differential equations. *Nonlinear Dyn.* **113**, 26603-26630 (2025).

[72] Deresse, A.T., Bekela, A.S. & Dufera, T.T. Leveraging Advanced Deep Neural Networks Algorithm for Solving Multi-dimensional Forward and Inverse Problems of Klein-Gordon Equation with Quadratic, Cubic, and Fifth-Degree Polynomials Nonlinearity. *Comput Math Model* (2025). https://doi.org/10.1007/s10598-025-09642-y

[73] Deresse, A.T., Dufera, T.T. & Firdi, M.D. Leveraging enhanced physics-informed neural networks based on adaptive weight loss for solving inverse problems of nonlinear Sine-Gordon equation. *Eur. Phys. J. Plus* **140**, 1155 (2025).

[74] Deresse, A.T., Bekela, A.S. A deep learning approach: physics-informed neural networks for solving a nonlinear telegraph equation with different boundary conditions. *BMC Res Notes* **18**, 77 (2025).

[75] Deresse, A.T., Dufera, T.T. A deep learning approach: Physics-informed neural networks for solving the 2D nonlinear Sine-Gordon equation. *Results Appl. Math.* **25**, 100532 (2025).

[76] Deresse, A.T., Dufera, T.T. Numerical solution of (2+1)-dimensional nonlinear sine-Gordon equation with variable coefficients by using an efficient deep learning approach. *Z. Angew. Math. Phys.* **76**, 134 (2025).

[77] Deresse, A.T., Dufera, T.T. Exploring Physics-Informed Neural Networks for the Generalized Nonlinear Sine-Gordon Equation. *Appl. Comput. Intelligence Soft Comput.* **2024**, 328977 (2024).

[78] Qasim, M., Yao, F. & Baber, M.Z. Exploring breather, M-lump, lump interaction, and rogue wave phenomena for the constant coefficients (2+1)-dimensional Graphene sheets equation via neural networking. *Nonlinear Dyn.* **113**, 28093-28118 (2025).

[79] Qasim, M., Fengping, Y. & Baber, M.Z. Explicit wave solutions profile of (3+1)-dimensional Bateman-Burgers equation via bilinear neural network method. *Eur. Phys. J. Plus* **140**, 224 (2025).

[80] Qasim, M., Yao, F. & Baber, M.Z. & Younas, U. Investigating the higher dimensional Kadomtsev-Petviashvili-Sawada-Kotera-Ramani equation: exploring the modulation instability, Jacobi elliptic and soliton solutions. *Phys. Scr.* **100**, 025215 (2025).

[81] Qasim, M., Yao, F. & Baber, M.Z. & Younas, U. Qualitative analysis and solitonic profiles of extended (3+1)-dimensional Kairat-X equation. *Eng. Comput.* **42**(6), 2179-2204 (2025).

[82] Alhakim, L., Gasmi, B., Moussa, A. & Mati, Y. Bifurcation, chaotic behavior, and soliton solutions of the Kairat-II equation via two analytical methods. *Partial Diff. Eq. Appl. Math.* **13**, 101135 (2025).

[83] Alhakim, L., Gasmi, B., Moussa, A., Mati, Y. & Baskonus, H.M. Exploring bifurcation, phase portraits, and exact solutions of the Fokas equation using the improved Cham method. *Partial Diff. Eq. Appl. Math.* **13**, 101134 (2025).

[84] Gasmi, B., Moussa, A., Mati, Y., Alhakim, L. & Akgül, A. Solving nonlinear partial differential equations using a novel Cham method. *J. Taibah Univ. Sci.* **17**, 2272728 (2023).

[85] Younas, U., Muhammad, J., Ismael, H.F., Sulaiman, T.A., Emadifar, H. & Ahmed, K.K. The New Combined Kairat-II-X Differential Equation: Diversity of Solitary Wave Structures via New Techniques. *J. Nonlinear Math. Phys.* **32**, 55 (2025).

[86] Younas, U., Muhammad, J., Ismael, H.F., Sulaiman, T.A., Emadifar, H. & Ahmed, K.K. Extended (3+1)-dimensional Kairat-II and Kairat-X equations: Painlevé integrability, multiple soliton solutions, lump solutions, and breather wave solutions. *Int. J. Num. Meth. Heat Fluid Flow* **34**(5), 2177-2194 (2024).

[87] Rizvi, S.T.R., Jlali, L., Anjum, I., Abad, H., Solouma, E. & Seadawy, A.R. Nonlinear Stochastic Wave Behavior: Soliton Solutions and Energy Analysis of Kairat-II and Kairat-X Systems. *Frac. Fract.* **9**, 728 (2025).

[88] Mathanaranjan, T. Lie Symmetries, Soliton Solutions, Conservation Laws, and Stability Analysis of the Combined Kairat-II-X Equation. *Math. Meth. Appl. Sci.* **48**(18), 16722-16729 (2025).

[89] Mehanna, M.S. & Wazwaz, A.M. Tri-analytical approach to Kairat-II and Kairat-X equations. *Rom. Rep. Phys.* 1-19 (2025).

[90] Demirbilek, U., Tedjani, A.H. & Seadawy, A.R. Analytical solutions of the combined Kairat-II-X equation: a dynamical perspective on bifurcation, chaos, energy, and sensitivity. *AIMS Math.* **10**(6): 13664-13691 (2025).